Summertime Influence of SST on Surface Wind Stress off the U.S. West Coast from the U.S. Navy COAMPS Model*

TRACY HAACK

Marine Meteorology Division, Naval Research Laboratory, Monterey, California

DUDLEY CHELTON

College of Oceanic and Atmospheric Sciences, Oregon State University, Corvallis, Oregon

JULIE PULLEN AND JAMES D. DOYLE

Marine Meteorology Division, Naval Research Laboratory, Monterey, California

MICHAEL SCHLAX

College of Oceanic and Atmospheric Sciences, Oregon State University, Corvallis, Oregon

(Manuscript received 2 July 2007, in final form 24 April 2008)

ABSTRACT

High-resolution mesoscale model sea surface temperature (SST) analyses and surface wind stress forecasts off the U.S. West Coast are analyzed on monthly time scales for robust signatures of air–sea interaction as the surface winds encounter ocean surface features such as SST fronts, filaments, and eddies. This interaction is manifest by the linear relationship, or coupling coefficient, between the downwind SST gradient and wind stress divergence and between the crosswind SST gradient and wind stress curl evident from analysis of fields averaged over 29 days. This study examines fields from the Coupled Ocean–Atmosphere Mesoscale Prediction System (COAMPS) model, spanning the summer months, June–September, for four consecutive years, 2002–05. Relative to several models evaluated previously, coupling coefficients are much closer to those calculated from Quick Scatterometer (QuikSCAT) satellite measurements. In addition, the summertime correlation between the wind stress derivative field and its corresponding SST gradient field on monthly time scales agrees well with satellite-derived correlations. Sensible and latent heat flux fields are also analyzed for features indicative of pronounced air–sea exchange associated with SST influence.

1. Introduction

Coupling between the ocean and atmosphere is greatly enhanced where there are strong sea surface temperature (SST) fronts. As noted by Mooers and Robinson (1984) and many subsequent studies, the California (CA) Current comprises an equatorward jet with many embedded turbulent filaments, eddies, and meanders creating small-scale SST features. Considerable mesoscale variability develops in the CA Current from spring to fall as the jet moves offshore (Strub and James 2000; Castelao et al. 2006). A recent study by Chelton et al. (2007, hereafter CSS07) identified strong influences of the CA Current's SST distribution on the surface wind stress in summertime from satellite data. In that study, indications of ocean–atmosphere interaction are manifest as small-scale structures in the wind stress curl and divergence fields, which are linearly related to the crosswind and downwind SST gradients, respectively. The slopes, or coupling coefficients, from these linear relationships quantify the intensity of the air–sea exchange.

The observed coupling results from the atmosphere's response to a change in SST, whereby the wind speed

* COAMPS is a registered trademark of the Naval Research Laboratory.

Corresponding author address: Tracy Haack, Naval Research Laboratory, Marine Meteorology Division, Monterey, CA 93943-5502.
E-mail: haack@nrlmry.navy.mil

DOI: 10.1175/2008JPO3870.1

decelerates over colder water and accelerates over warmer water. This SST influence on surface winds was first suggested by Sweet et al. (1981) and subsequently by Jury and Walker (1988), Wallace et al. (1989), Hayes et al. (1989), and Friehe et al. (1991). Numerous recent studies have documented this response from satellite observations over strong SST fronts throughout the world's oceans (see reviews by Xie 2004; Chelton et al. 2004; Small et al. 2008). Previous evaluations of mesoscale, global, and climate numerical model forecasts, however, indicate that the models underrepresent the small-scale (~25 km) interaction between the ocean and atmosphere. Coupling coefficients are only about half, or less, of those inferred from satellite observations (Chelton 2005; Maloney and Chelton 2006; Chelton et al. 2007; Seo et al. 2007).

This study documents the degree to which the U.S. Navy's nonhydrostatic atmospheric mesoscale model, Coupled Ocean–Atmosphere Mesoscale Prediction System (COAMPS), reproduces the observed signatures of air–sea coupling found by CSS07 over four upwelling seasons. Evidence of one-way coupling in COAMPS has previously been noted by Haack et al. (2005). Spatial distributions of monthly mean SST for July 1999 contained small-scale features associated with mesoscale eddies and filaments and, in some locations, variations were linked to those of mean wind stress curl and near-surface wind speed. Here we expand upon those early results, examining COAMPS analysis and forecast fields over the same 2002–05 upwelling seasons, as in CSS07. Although we evaluate hourly (or 12 hourly) fluctuations, the focus is primarily on monthly time scales utilizing a 29-day averaging period. The length of the averaging period is considered in detail by CSS07 (their Figs. 11 and 12) who show that air–sea coupling becomes evident with averaging of 10 days or more. Much of the variability in the wind stress is on shorter daily or weekly time scales driven by diurnal and synoptic forcing; however, the emphasis here is on longer time scales on which SST forcing is the dominant mechanism for small-scale variability in the surface wind field.

The high-resolution model fields are also exploited to address some of the limitations in CSS07. The monthly mean of the COAMPS SST analysis at 9-km grid spacing affords considerable improvement over that of the 56-km footprint of the Advanced Microwave Scanning Radiometer (AMSR) satellite data used by CSS07. Furthermore, the Quick Scatterometer (QuikSCAT) is unable to measure winds closer than about 30 km from land, and AMSR is unable to measure SST closer than about 75 km from land, extending to 50 and 100 km in the derivative and gradient fields of interest here, and buoy data are too sparsely distributed to assess spatial variability. Utilizing COAMPS fields we are also able to evaluate air–sea interaction within the 100-km-wide coastal zone, which is beyond the reach of satellite measurements.

We present the bulk of our findings in section 4, describing the 4-yr mean summertime statistics, and, in section 5, documented the air–sea interaction features from COAMPS. These two sections are preceded by a summary of the modeling system and forecast design in section 2 and a summary of the analysis methodology with examples in section 3. Discussions of additional findings are presented in section 6, and we conclude in section 7.

2. Modeling system and forecast design

The COAMPS U.S. West Coast nested domain (81, 27, and 9 km grid spacing) has been running in near real time since 1998, supplemented by reanalyses when necessary to form the continuous 4-yr-long set of fields used in this study between the years 2002 and 2005. During this time, the code has been subject to periodic upgrades as improvements are tested and incorporated into the system. The details of the model and system have been reported elsewhere (Hodur 1997). Of primary interest here are advancements made to the model's surface flux code, described by Wang et al. (2002), that modify the original Louis et al. (1982) parameterization based on data from the Tropical Ocean and Global Atmosphere Coupled Ocean–Atmosphere Response Experiment (TOGA COARE) (Fairall et al. 1996).

A few papers have considered the COAMPS fully coupled air–sea capability, including a variety of idealized studies (Haack and Hodur 1996; Hodur 1997; Perlin et al. 2007; Spall 2007), and the first real-data coupled forecasts over the Adriatic Sea (Pullen et al. 2006, 2007). However, most COAMPS forecasts have been conducted with an uncoupled atmospheric model using a SST analysis field at the atmosphere's lower ocean boundary, as is the case here. The accuracy and resolution of COAMPS SST fields are critical to resolving the scales of variability that are important in ocean–atmosphere interaction, while confining our analysis to an uncoupled scenario allows us to isolate the specific influence of SST on the overlying atmosphere.

Real-data COAMPS case studies take advantage of 12-hourly updated SST derived from an optimum interpolation (OI) analysis performed on the 9-km model grid (Cummings 2005). The SST analysis is designed to incorporate data from multiple infrared and microwave satellite observing platforms; for this study, only the

8-km resolution Advanced Very High Resolution Radiometer (AVHRR) SST retrievals from cloud-free pixels are used, augmented with buoy, ship, and Coastal-Marine Automated Network (C-MAN) station SST data. Since the grid spacing is very near that of the primary observing system, much of the mesoscale detail observed by satellite is retained in the SST analysis.

Despite widespread summertime stratus, the analysis captures oceanic features including local effects near coastal promontories and SST frontal features offshore because of sequential cycling of the SST analysis and the incremental update procedure. This method provides a time history that retains the structure of the previous analysis, supplemented with observationally based corrections collected over a 24-h window. Climatology is introduced as an observation if the "age of the data," which is based on the number of hours since the grid point has been influenced by an observation, is greater than ~10 days. The month-long averaging period used in this study mitigates the impact of occasionally sparse satellite data during periods of persistent cloudiness. The SST corrections are distributed spatially by background-error covariances over a horizontal length scale specified by the local first baroclinic Rossby radius of deformation plus the grid spacing scaled by a proportionality constant (Cummings 2005). Careful treatment of background- and observation-error covariances yields analyses for the CA Current region with considerable mesoscale detail, as shown in Figs. 2–5. The veracity of the 29-day-averaged COAMPS SST fields is evident from the very close agreement between the structures of the SST gradient fields and the wind stress curl and divergence fields constructed from the entirely independent QuikSCAT observations of wind stress (see Fig. 2).

COAMPS triply nested domain for the U.S. West Coast (Fig. 1) is run in sequential incremental update mode to produce the hourly fields used in this study. Lateral boundary conditions are supplied by the Navy Operational Global Atmospheric Prediction System (NOGAPS) on the outermost 81-km grid every 6 h (Hogan and Rosmond 1991). At 12-h intervals, the first guess fields from the previous 12-h forecast are adjusted by observation analysis increments derived from a three-dimensional multivariate OI analysis (Barker 1992). In this manner, mesoscale detail and vertical gradients are maintained while allowing for quality-controlled observations to correct the initial fields (Baker 1992). Sequential updates also maintain continuity, so there are no sharp discontinuities or spinup adjustments across successive forecasts.

Most of the overwater, near-surface atmospheric observations consist of ship and buoy data (approximately

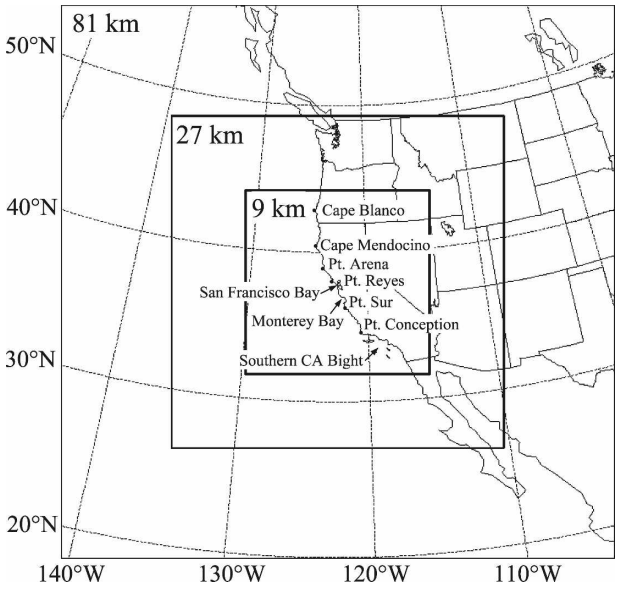

FIG. 1. COAMPS triply nested U.S. West Coast model grids (81-, 27-, 9-km grid spacing), labeled with geographical locations of interest.

25 observations over the inner grid) and Special Sensor Microwave Imager (SSM/I) wind speeds (0–250 observations over the inner grid). Surface reports of sea level pressure and air temperature are converted to observations of 1000-mb height, and wind speed and direction is decomposed into 1000-mb zonal and meridional wind components (Phoebus and Goerss 1992). Upper-air data, such as satellite observations of water vapor, winds, and automated aircraft reports, are also assimilated into COAMPS analysis, and through vertical correlations their influence can spread to lower model levels. QuikSCAT wind speeds are thinned and averaged to 50-km spacing and assimilated in the outermost 81-km grid analysis (250–750 observations over the outer grid), but these data have been found to have a barely detectable impact on the surface wind fields in operational weather forecasts and analyses, which evidently grossly underutilize the information content of QuikSCAT data (Chelton and Freilich 2005; Chelton et al. 2006).

For this study, the atmospheric model contains 40 vertically stretched levels and the lowest 1 km has vertical grid spacing of 100 m or less. Here we focus on the impact of the 12-hourly updated SST analyses on the surface wind stress field, which is a function of the wind speed and direction at the lowest model level (10 m). The small-scale air–sea interaction becomes apparent by examining the derivatives of monthly averaged SST and wind stress fields, as described in the next section. Throughout this paper, *monthly average* refers to a

29-day average, *mean* refers to the 4-yr summertime mean, and the terms *coupling* and *interaction* refer to the one-way influence of analyzed SST on the COAMPS atmospheric surface layer.

3. Methodology and examples of upwelling evolution

We compute statistics using procedures that CSS07 applied to QuikSCAT and AMSR observations. Wind stress curl (WSC) and wind stress divergence (WSD) fields are formed from hourly wind stress forecasts. The SST gradient is decomposed into crosswind ($|\nabla \mathrm{SST}| \sin\Delta\theta$)and downwind ($|\nabla \mathrm{SST}| \cos\Delta\theta$) components, where $\Delta\theta$ is the angle between the SST gradient vector and the wind stress vector. Crosswind SST gradients (CWSST) are amplified where the SST gradient has little variation in the direction of the stress vector, and downwind SST gradients (DWSST) are greatest where the SST variation is largest in the direction of the stress vector. The cross- and downwind directions are determined from hourly variations in the wind stress vector; thus, the CWSST and DWSST fields also vary hourly, although the SST gradient field itself is fixed over each 12-h period.

The 29-day averaging period is used here for consistency with CSS07 to highlight the impact of slowly varying SSTs on surface winds. The averages are computed from successive 1–12-h forecasts with center dates between 1 June and 30 September for years 2002–05. They are staggered by 7 days so that a total of 72 overlapping 29-day averages cover the 4-yr span of this study. Figure 2 shows two examples of 29-day-average SST, wind stress, WSC with contours of CWSST overlaid, and WSD with contours of DWSST overlaid: one for a center date at the beginning of the 2004 upwelling season (Fig. 2a) and the other at the end (Fig. 2c). The correspondence between wind stress and SST becomes much more apparent later in the season as SST fronts become strengthened and extend farther offshore. Wind stresses are locally reduced over colder SST squirts and jets and enhanced over warm SST. The linkage between the wind stress derivative fields and SST gradient field reveals strong interaction at small scales both early and late in the season. Regions of negative (positive) WSC occur over regions of negative (positive) CWSST, as is also the case for WSD and DWSST.

To emphasize the link between small-scale features in the model and observations, QuikSCAT-derived wind stress fields are also shown with COAMPS analyzed SST in Figs. 2b and 2d. This remarkable correspondence would only be possible for a SST analysis that captures the details of oceanic features responsible for the observed variability in the wind field. In comparing 29-day averages of SST and gradient magnitudes to those obtained by CSS07 from AMSR satellite data, the COAMPS analysis produces greater cross- and downwind SST gradient magnitudes owing to better horizontal resolution. The consistency between model and observations is not limited to this particular example. There is close correspondence in 29-day averages spanning all four of the summertime periods considered here.

The seasonal evolution of the synoptic pressure pattern over the U. S. West Coast establishes the wind forcing that drives coastal upwelling, extending from May through September. It begins with periods of intense springtime winds that span the length of the coast between Cape Blanco and Point Conception. As the season progresses, the broad wind speed maximum shifts northward, weakens, and becomes more localized. Thus, as discussed by Marchesiello et al. (2003) and found in observations (Strub and James 2000), peak wind-driven upwelling occurs along the central and southern California coasts in spring but contracts to the northern California coast in summer. Along with upwelling, strong SST gradients concurrently shift northward with the low-level wind forcing. Hence, the southern portion of the domain exhibits greater variability and small-scale structure for the 13 June 2004 center date (Fig. 2a), while the northern portion contains greater structure for the 5 September 2004 center date (Fig. 2c). Regions of strong SST gradients generate enhanced air–sea interaction and a pronounced impact on the overlying wind stress derivative fields.

One-dimensional sections extending west from the coast at San Francisco Bay (near 37.75°N) for three 29-day averages show the evolution of the SST and wind stress fields near the beginning, middle, and end of the upwelling season (Fig. 3). The wind stress and SSTs are out of phase west of the wind stress peak and in phase to its east, as demarcated by the dotted vertical lines in Fig. 3. The shoreward reduction in wind stress that occurs over cold coastal waters is commonly associated with the formation of an internal atmospheric boundary layer, as discussed by Mahrt et al. (2004) and modeled by Perlin et al. (2007).

Where the wind stress and SSTs are in phase, derivatives of the wind stress and gradients of the SSTs are strongly amplified. Early in the upwelling season the wind stress peak moves westward and the region where SST gradients are intensified expands. The most striking features in these sections are the cross- and downwind SST gradient magnitudes that vary in concert with the WSC and WSD fields, respectively, for all center dates and locations except the 20 km closest to shore,

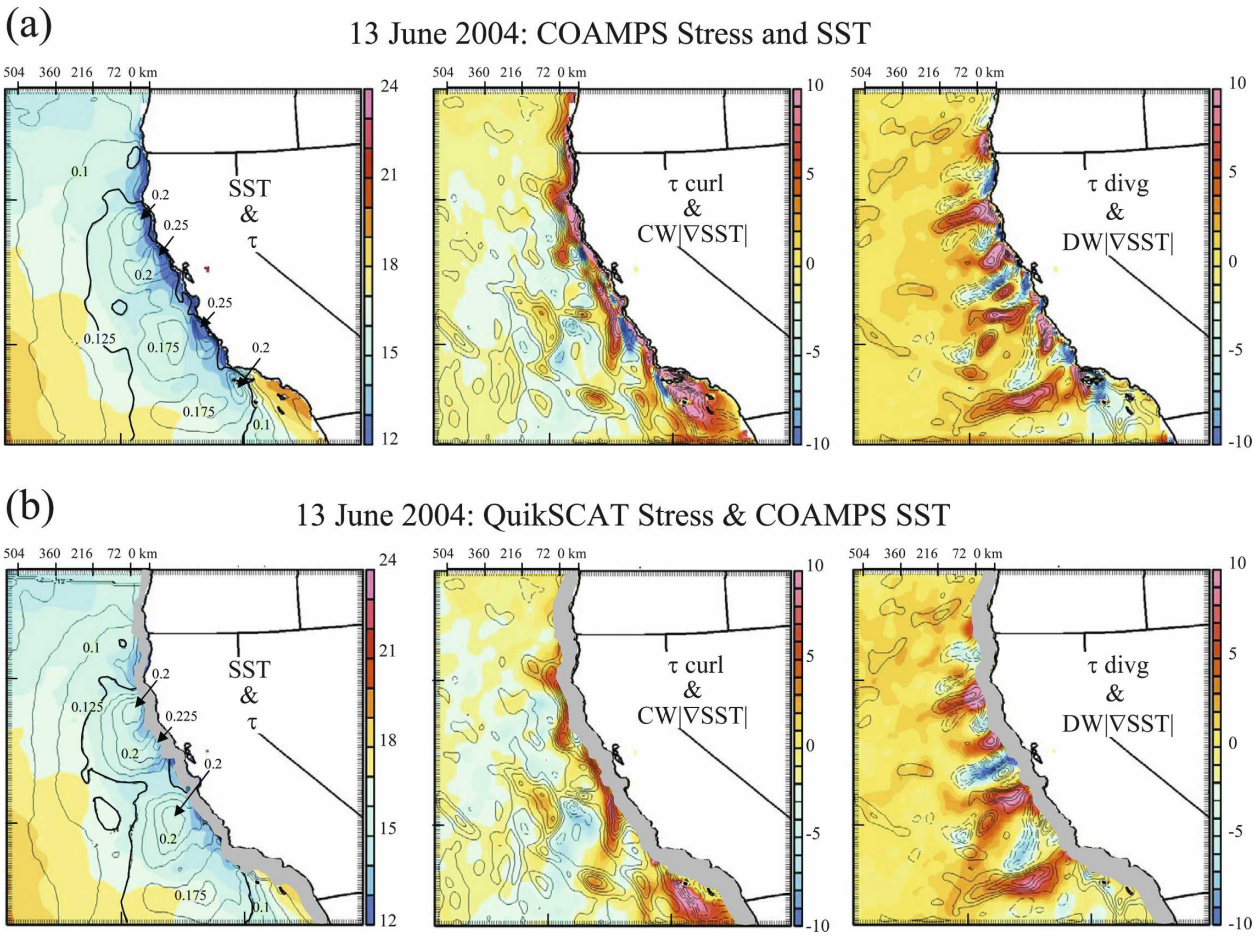

FIG. 2. Example 29-day averages for center dates (a), (b) 13 Jun 2004 and (c), (d) 5 Sep 2004. Panels in (a) and (c) [(b) and (d)] are derived from COAMPS [QuikSCAT] wind stress and SST fields: gray shading masks the region without satellite data. (left) SST (°C, color shading) and wind stress (N m^{-2}, contour interval of 0.25). (middle) Wind stress curl [N m^{-2} $(10^4$ km$)^{-1}$, color shading] and crosswind SST gradient [°C (100 km)$^{-1}$, contour interval of 0.5]. (right) Wind stress divergence [N m^{-2} $(10^4$ km$)^{-1}$, color shading] and downwind SST gradient [°C (100 km)$^{-1}$, contour interval of 0.5]. Negative contours are dashed and positive contours solid.

where the correspondence is likely disrupted by orographic effects. This clearly indicates that, over the open ocean during the upwelling season, substantial SST variability is contained in COAMPS analyses and this SST variability has a significant impact on the atmospheric surface layer of the model.

4. Summertime mean fields

To examine the mean fields, aggregate statistics are computed by concatenating the overlapping 29-day-average fields over the four June–September summertime periods from 2002 to 2005 to produce a summertime average and standard deviation (STD). Fluctuations on monthly time scales are given by the deviations of the 29-day averages from the mean. Fluctuations on shorter time scales are given by the deviation of the hourly fields (or 12-hourly fields for SST) from the mean.

a. Sea surface temperature

The SST analysis composite field shows a mean pattern of coastal upwelling with 2–3°C colder water extending about 175 km from shore between Cape Blanco and San Francisco Bay, narrowing to about 100 km on the central coast north of Point Conception (Fig. 4a). The magnitude of the mean SST gradient is largest within this zone [3°–5°C (100 km)$^{-1}$] but contains considerably greater heterogeneity extending farther offshore than is evident in the SST field (Fig. 4b). The large-scale features in the gradient field correspond well to those derived by Castelao et al. (2006) from Geostationary Operational Environmental Satellite (GOES) data who show the seasonal evolution from

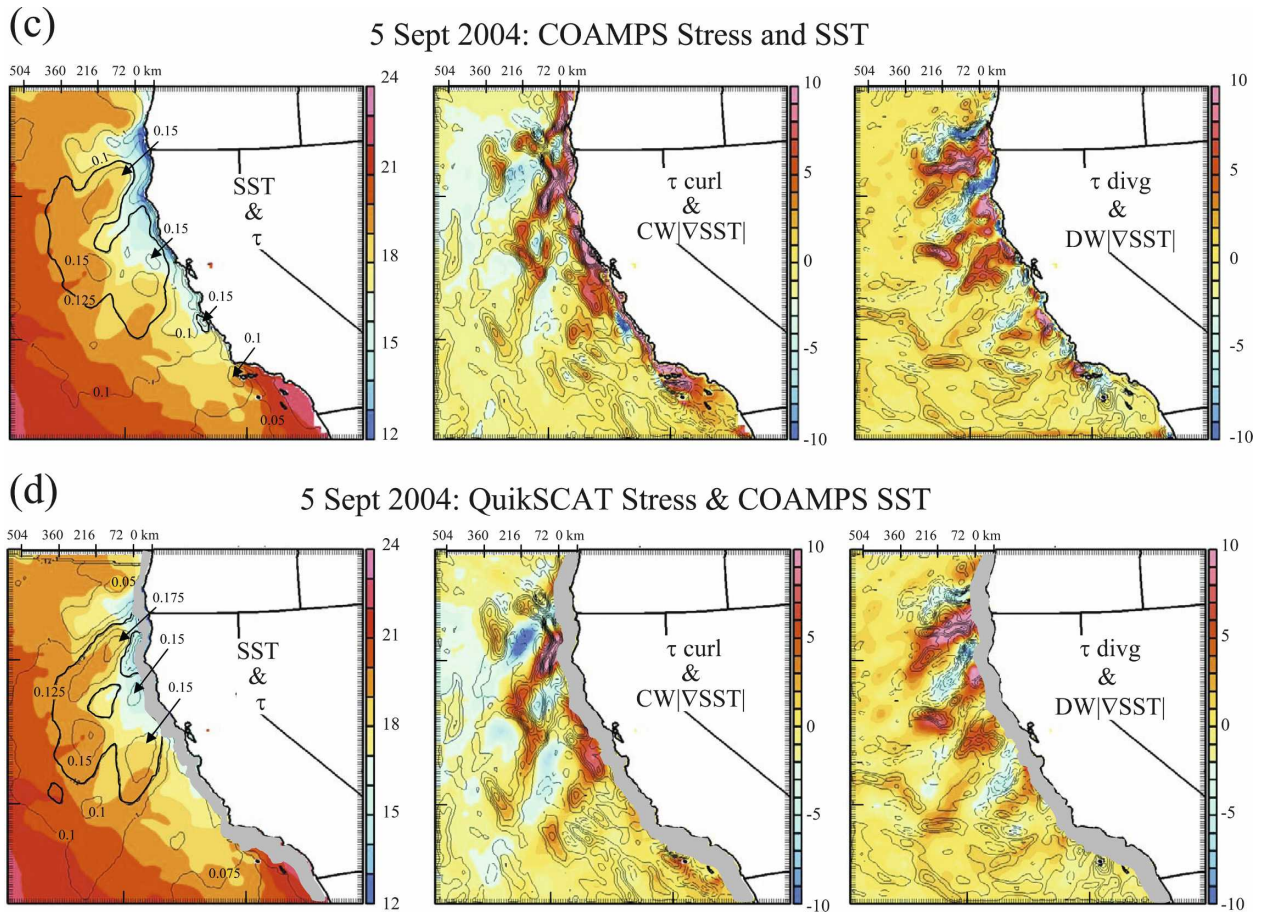

FIG. 2. (*Continued*)

2-month averages for years 2001 to 2004. In both observations and model, the strongest magnitudes shift northward from spring to summer, occur in summer months between latitudes 38° and 45°N, and are three times greater in the 100-km nearshore region than farther offshore.

The SST standard deviations, computed from both the 12-hourly deviations (Fig. 4c) and from the overlapping 29-day averages (Fig. 4e), span a narrow range between 1° and 2°C and are quite consistent in pattern between the two anomaly fields. The greatest variance nearshore occurs between promontories in regions prone to both strong upwelling and occasional intrusions of warm SST (e.g., north of Cape Blanco, between Cape Blanco and Cape Mendocino, and near Point Reyes). Regions of lower variance coincide with more persistent SST features such as the cold filaments that often move west offshore of Cape Blanco and Point Arena and the warm intrusion from the southwest offshore of Point Sur. As noted in subsequent sections, many small-scale features in the wind stress and surface flux fields are linked to the SST, thereby implying interaction between the ocean and atmosphere.

The SST gradient magnitude and its standard deviation clearly reveal the spatial structure and variability associated with SST fronts and meanders (Figs. 4b,d). The STD of SST gradient magnitudes obtained from AMSR data by CSS07 are reproduced in Fig. 4f for comparison with COAMPS (Fig. 4d). (Note the 100-km band nearshore within which the gradients of the SST field cannot be computed from AMSR because of land contamination in the antenna sidelobes.) COAMPS SSTs are consistent with AMSR, revealing broader maxima north of Point Reyes, but have considerably greater spatial structure and variability than the 56-km resolution features resolved from AMSR data. Reduced variance in the western portion of the domain is in good agreement with values computed from satellite data.

The cross- and downwind SST gradient magnitude fields reveal structure in the analyzed mean fields along an across the mean equatorward stress vector, respectively (Figs. 5a,b). Because of persistent northwesterly

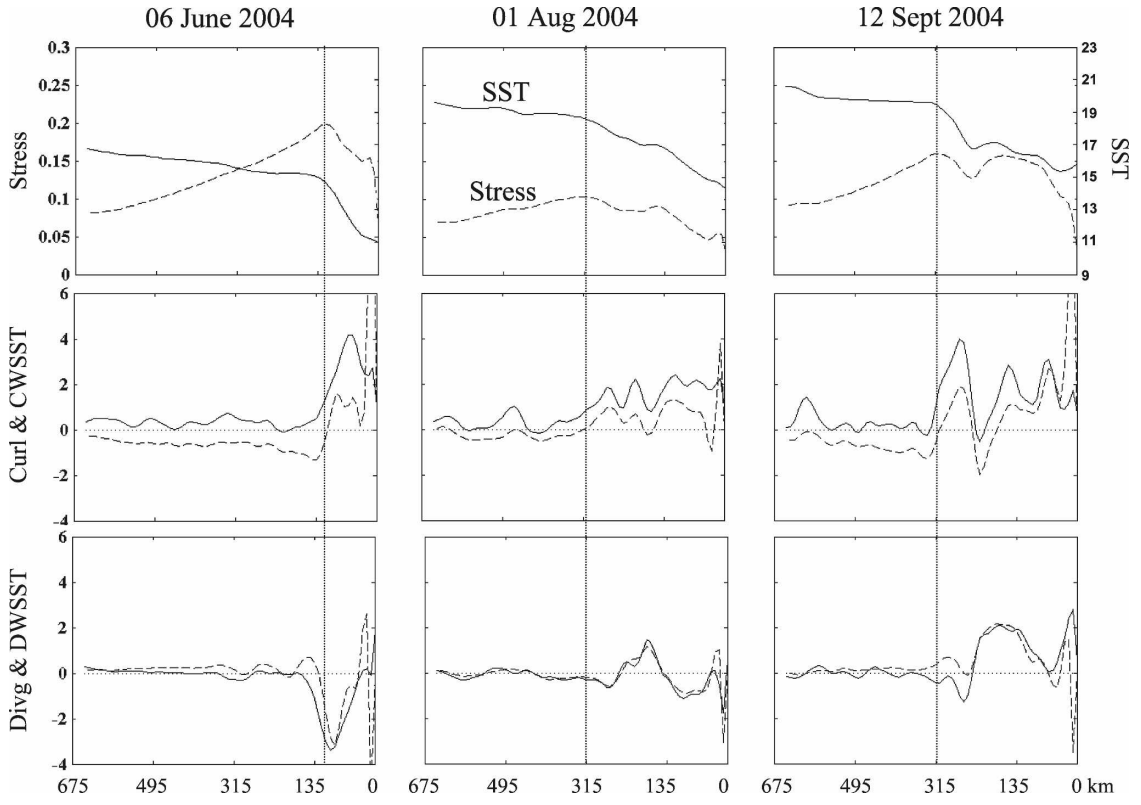

FIG. 3. East–west section extending west from the coast at San Francisco Bay along latitude 37.75°N from 29-day averages for center dates (left) 6 Jun 2004, (middle) 1 Aug 2004, and (right) 12 Sep 2004: (top to bottom) SST (K, solid) and wind stress (N m^{-2}, dashed), crosswind SST gradient [°C (100 km)$^{-1}$, solid] and wind stress curl [N m^{-2} (10^4 km)$^{-1}$, dashed], and downwind SST gradient [°C (100 km)$^{-1}$, solid] and wind stress divergence [N m^{-2} (10^4 km)$^{-1}$, dashed]. The vertical dotted lines denote the wind stress peak.

winds and coastal upwelling along most of the U.S. West Coast in summer, maxima in CWSST occur within 100 km of the coast and values are generally positive across the model domain since the SST increases nearly monotonically offshore. In contrast, DWSSTs are intensified when SST features (meanders, fronts, filaments, and jets) are oriented at angles oblique to the prevailing wind direction. Figure 5b shows alternating regions of strong negative/positive DWSST at coastal headlands extending southwestward, which denote preferential locations of cold SST fingers (dashed lines in Fig. 5b). As noted in the next section, these cold filaments produce a convergent wind stress on the upwind side and a divergent one on the downwind side. These features are only apparent in the gradient field, whereas the mean SST field in Fig. 4a is considerably smoother.

Variance of the SST gradient fields, computed from both the hourly fields (Figs. 5c,d) and from the overlapping 29-day averages (Figs. 5e,f), also reveal considerable spatial structure. In the near coastal zone monthly deviations are about half the magnitude of hourly deviations due to diurnal changes in the direction of the wind stress vector that alter the downwind and crosswind directions. However, there is little difference in pattern and spatial structure between the two sets of anomalies for SST fields beyond about 100 km from the coast. The similarity between daily and monthly variance is in sharp contrast to that of the wind stress derivative fields described in the next section (Figs. 7c,d and 7g,h).

b. Wind stress

The mean wind stress is driven by factors other than SST, in particular by the depth of the marine atmospheric boundary layer (MABL) and by changes in the large-scale pressure field. From spring into early summer, the large-scale mean sea level (MSL) pressure gradient weakens and the subtropical high pressure cell shifts north. Consequently, the atmospheric low-level jet in the summertime mean is stronger off the north coast than off the central and south coasts. The offshore Ekman transport and coastal upwelling associated with these strong winds produces the coldest SST in this

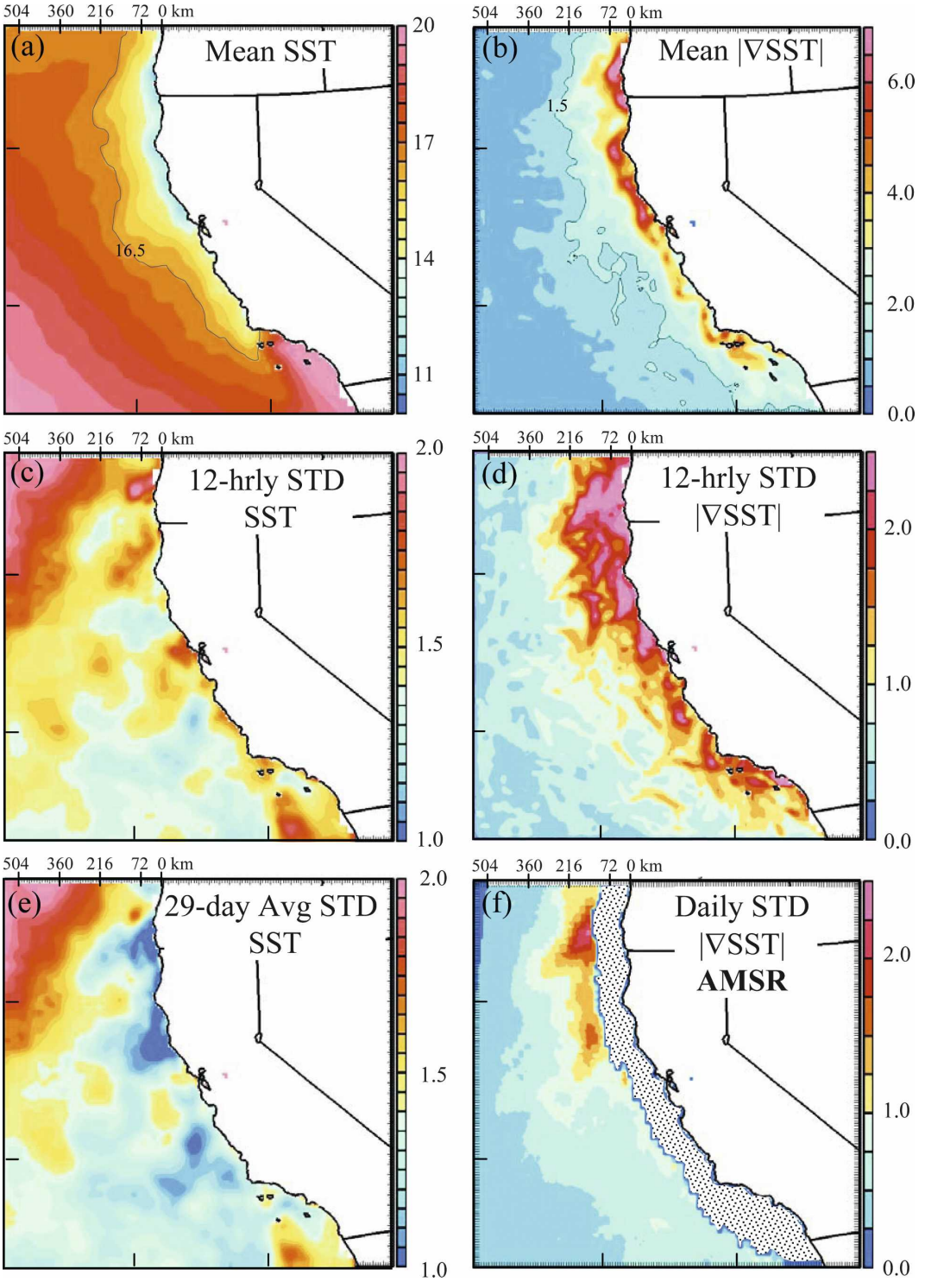

FIG. 4. SST and SST gradient magnitude means and standard deviations (STDs), (left) SST (°C) and (right) SST gradient magnitude [°C (100 km)$^{-1}$]: (top to bottom) mean, 12-hourly STD, and 29-day average STD; [(bottom right) daily averaged SST gradient magnitude STD from AMSR for comparison with (d)]. The stippled area along the coast in (f) masks the region without satellite data

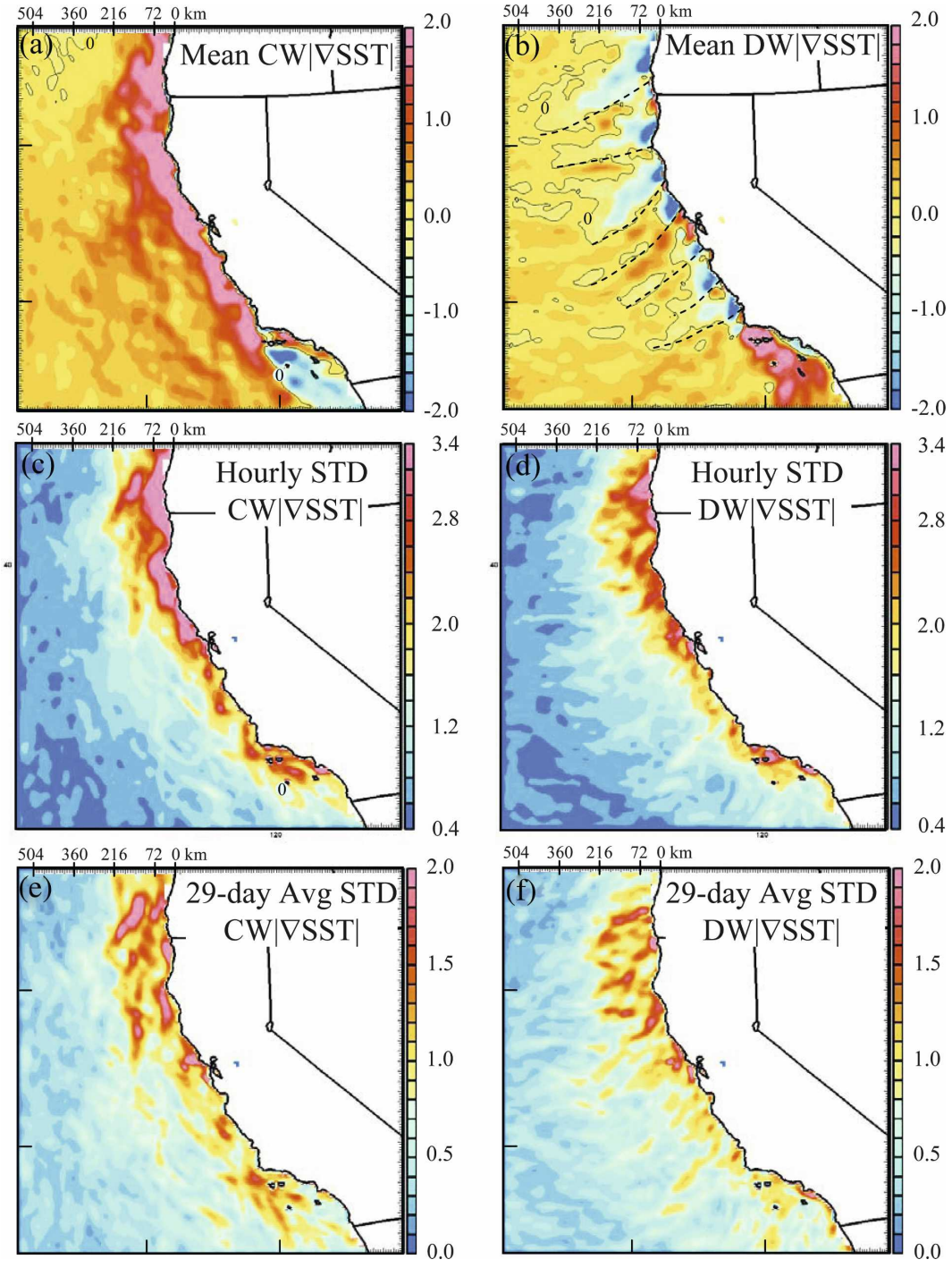

FIG. 5. SST gradient magnitude means and STDs [°C (100 km)$^{-1}$], (left) crosswind and (right) downwind: (top to bottom) mean, hourly STD, and 29-day-average STD. Dashed lines in (b) are mentioned in the text.

region (Fig. 4a). Near the coast, low-level winds are topographically enhanced or diminished by the hydraulic response of an inversion-capped MABL to bends in the steep mountainous coastline (Dorman 1985; Winant et al. 1988). Adopting terminology from fluid dynamics, zones of abrupt deceleration and MABL deepening are called "compression jumps" and zones of rapid acceleration and MABL thinning are called "expansion fans." These features typify the atmospheric response to a bend in the blocking orography in sum-

mertime (Burk et al. 1999; Edwards et al. 2001). We discuss in section 6 the implications of this topographic forcing on air–sea coupling signatures in the coastal zone as compared to offshore.

Wind stress standard deviations of the hourly fields (Fig. 6b) share the same pattern as the mean field with the largest fluctuations occurring in expansion fans associated with sea/land breeze forcing. Kindle et al. (2002) has documented the temporal variability in winds over the diurnal cycle in summer from 9-km COAMPS forecasts. It is noteworthy that the variance drops off more rapidly with distance from the coast than those in the daily averaged QuikSCAT fields analyzed by CSS07 (their Fig. 14). The monthly wind stress STDs (Fig. 6c) are similar to the hourly STDs in that they have the same five coastal peaks downwind of promontories, but the broad region of high variance in the southern portion of the domain differs from the hourly pattern. This difference can be explained by the northward progression of the subtropical high pressure cell early in the season, leaving diminished winds along the central and southern coasts. The contraction to the north coast of the mean, large-scale, low-level jet affects locations within the domain of the strongest SST gradients as well as the region of greatest air–sea interaction. The monthly wind stress variance also suggests a correspondence to the SST field. For example, the westward bulge in the wind stress STD offshore of the primary expansion fans near Cape Blanco, Cape Mendocino, and Point Sur is collocated with warm SST intrusions drawn shoreward (Fig. 4a). These fluctuations have an effect on surface heat flux variances discussed in section 5c.

The small-scale structure of the mean wind stress is more apparent in the derivative fields of WSC and WSD (Figs. 7a,b), as was the case with gradients of SST. Large variance near shore dominates the hourly fluctuations (Figs. 7c,d), in agreement with the daily averaged QuikSCAT fields (Figs. 7g,h), but variance in the model drops off more rapidly with distance from the coast. (Note the 50-km band near the coast where the derivatives for computing the WSC and WSD fields cannot be computed from QuikSCAT data because of land contamination in the antenna sidelobes.) The monthly wind stress derivative STD fields (Figs. 7e,f) contain about a third of the variance found in the hourly deviations and also diminish approximately 250 km away from the coast. This sharp reduction in variance offshore suggests that the model produces a weaker response to SST perturbations than that given in the analysis of satellite observations. Song et al. (2008) have shown from mesoscale atmospheric model simulations that underestimation of SST influence on

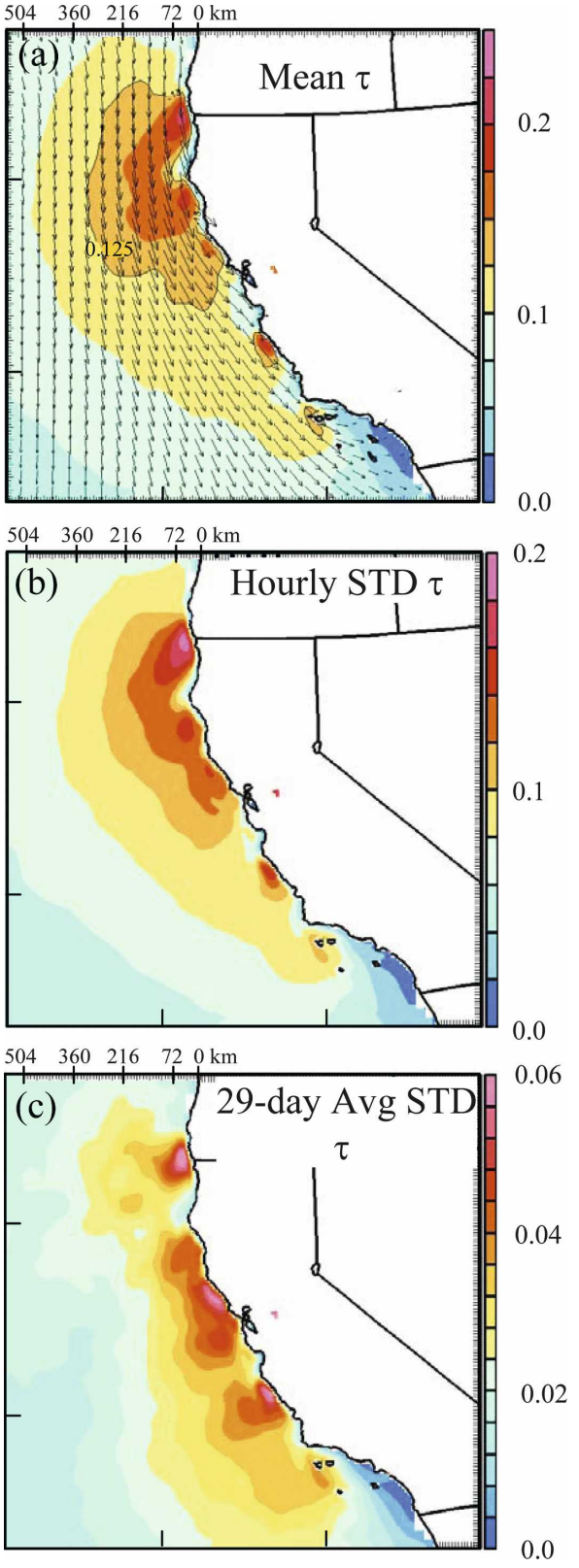

FIG. 6. Wind stress mean and STD (N m^{-2}): (top to bottom) mean, hourly STD, and 29-day-average STD.

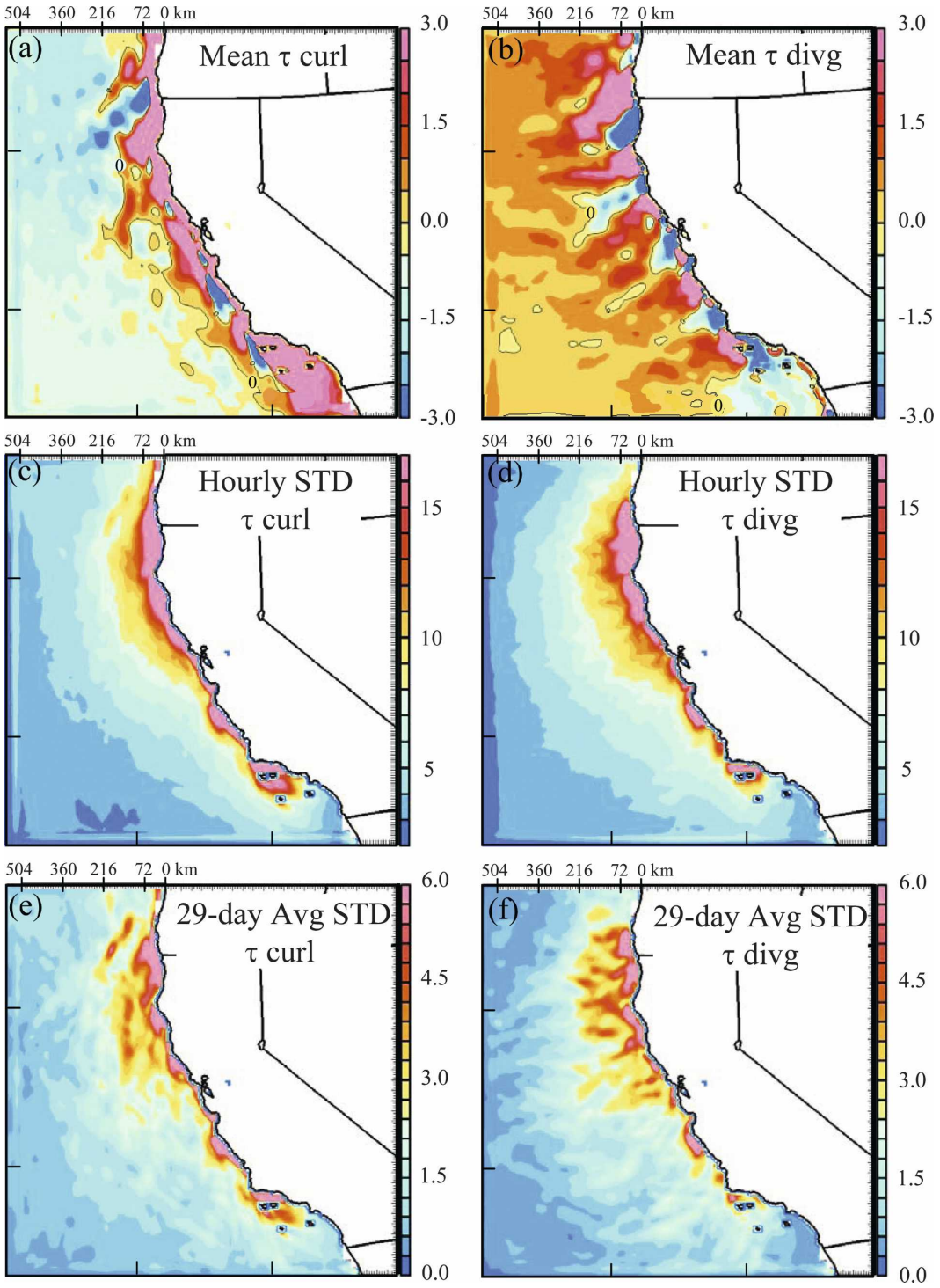

FIG. 7. Wind stress (left) curl and (right) divergence means and STDs [N m^{-2} (10^4 km)$^{-1}$]: (top to bottom) mean, hourly STD, 29-day-average STD, and QuikSCAT daily averaged wind stress curl and divergence STD [for (c),(d)]. The stippled area along the coast in (g),(h) masks the region without satellite data.

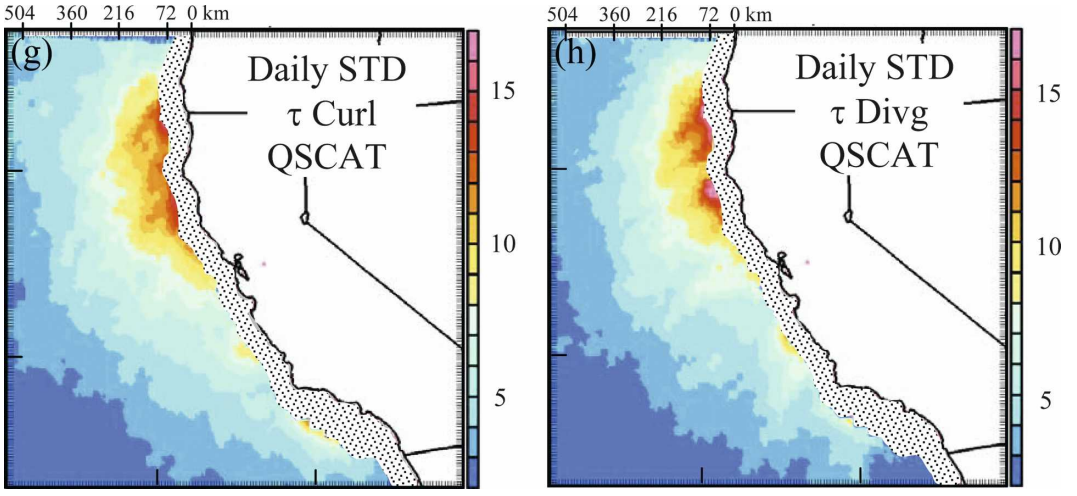

FIG. 7. (*Continued*)

surface winds is due primarily to underrepresentation of vertical mixing in the model in the unstable conditions usually found over the ocean.

To ascertain the influence of SST on WSC and the wind stress curl's potential for influencing SST, Ekman upwelling velocities were computed from both QuikSCAT (Fig. 8a) and COAMPS (Fig. 8b) WSC. In this figure, the mean distributions denote the large-scale forcing of the WSC field, while the 29-day-average anomaly distributions show the effect of SST-induced perturbation on WSC. COAMPS underestimates the dynamic range of the anomalies by about 20%, but they still represent an $O(1)$ perturbation of the large-scale WSC field. Thus, the SST drives variability in the wind stress curl that dynamically feeds back to the ocean in the form of upwelling and downwelling. Energetically, these perturbations contribute the equivalent of the large-scale forcing in establishing the WSC pattern and magnitudes. In section 6, we speculate further on potential atmospheric feedbacks to the ocean and the fully coupled nature of this region in summertime.

c. *QuikSCAT validation of COAMPS wind stress fields*

Validation of the COAMPS forecast wind stresses is provided by the QuikSCAT wind stress fields. Except near the coast where QuikSCAT is unable to measure the wind stress, the QuikSCAT data are considered "truth" for the purposes of assessing the COAMPS wind stress fields. There is no evidence of any systematic biases in QuikSCAT data (e.g., Chelton and Freilich 2005). To perform this verification, the 25-km footprint of the satellite data with twice-daily overpasses (near 0300 and 1400 UTC) and the correspond-

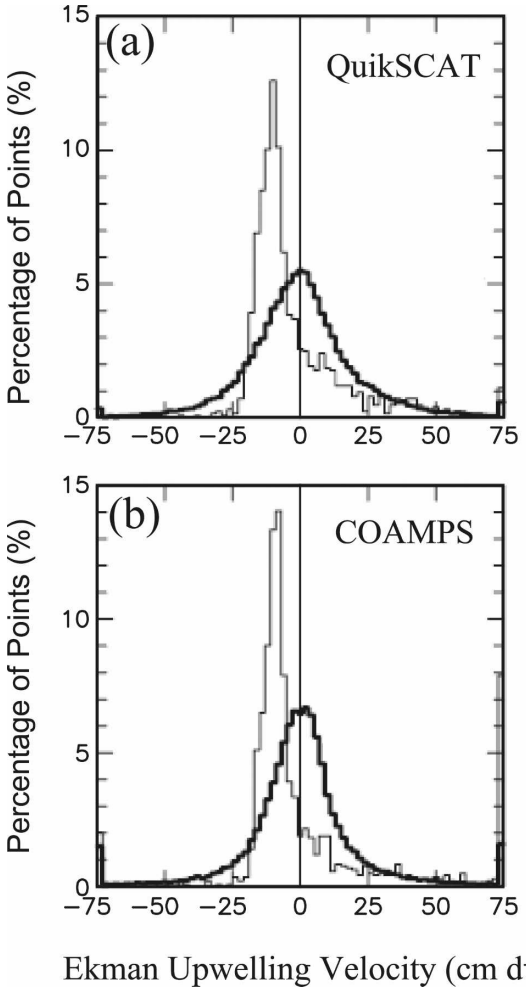

FIG. 8. Ekman upwelling velocity (cm day^{-1}) computed from (a) QuikSCAT-derived wind stress curl and (b) COAMPS-derived wind stress curl. The summertime mean is the gray line and the 29-day-average anomaly is the heavy black line. Distributions include points within the region shown in Fig. 12a.

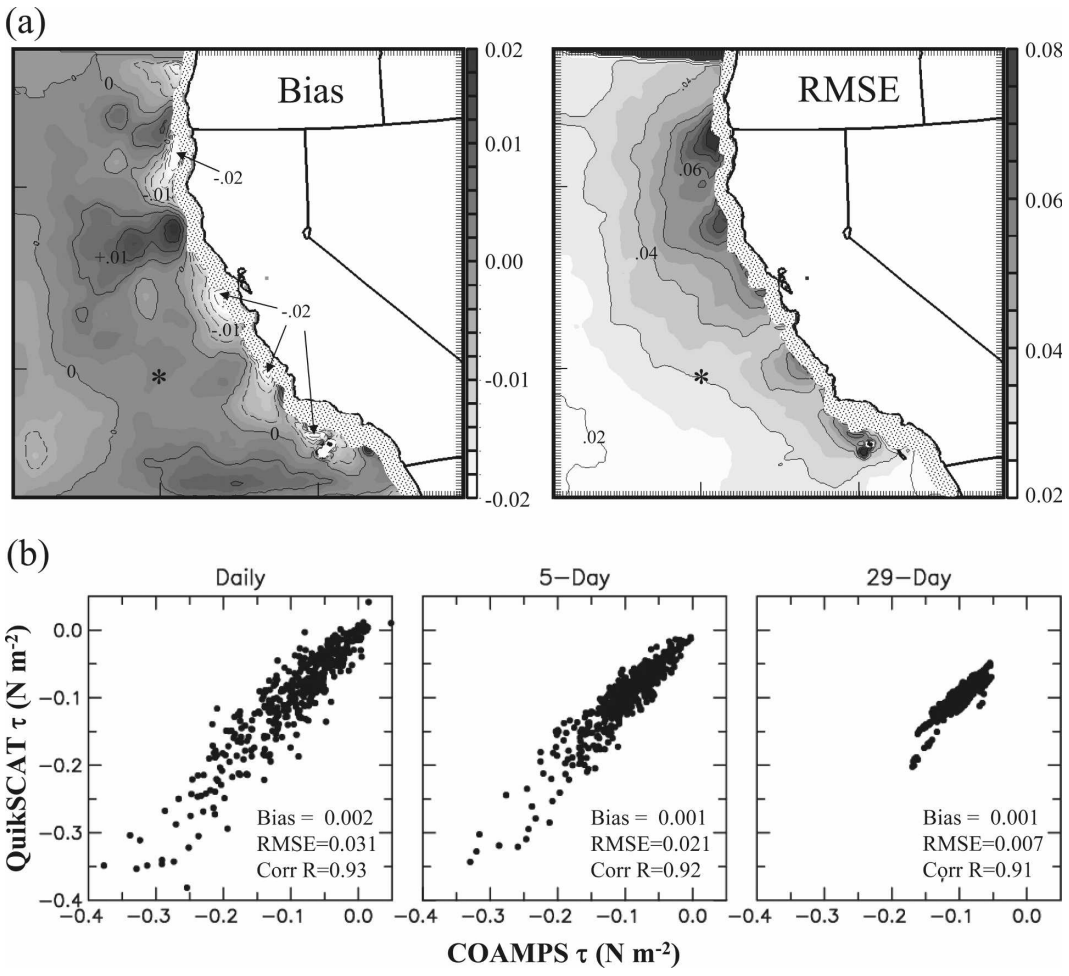

FIG. 9. (a) QuikSCAT − COAMPS mean difference and rms difference of daily averaged alongshore wind stress (N m^{-2}) (the stippled area along the coast masks the region without satellite data): (left) mean difference (contour interval 0.005, referred to as Bias) and (right) is rms difference (contour interval 0.01, referred to as RMSE). (b) Scatterplots of QuikSCAT and COAMPS alongshore wind stress (N m^{-2}) for three averaging periods at location denoted by an asterisk (35°N, 125°W). Values of Bias, RMSE, and correlation *R* are shown in (b) for reference.

ing model field (forecast time 0300 from the 0000 UTC forecast and 0200 from the 1200 UTC forecast) were interpolated to a common 0.25° × 0.25° grid and then daily averaged. At each grid point, the satellite − model mean difference and rms difference were computed from the daily averaged alongshore wind stress (Fig. 9a). For purposes of discussion, we use the terms *bias* and *error* (RMSE) below in describing the model differences from QuikSCAT.

The mean wind stress biases are nearly an order of magnitude less than the mean at most locations across the domain. There is a weak positive bias offshore of expansion fans and across much of the open ocean, indicating that overall COAMPS tends to underpredict the alongshore wind stress. The largest biases and RMSE occur along the coast, and errors are generally less than half the mean value. In a hydraulically controlled MABL, the transition from fast winds in expansion fans to blocked flow varies diurnally and is highly dependent on direction of the upwind flow and local pressure gradients (Haack et al. 2005) and so may not be captured sufficiently by twice-daily wind stress fields. Scatterplots of QuikSCAT to COAMPS alongshore wind stress at a point well offshore (asterisk in Fig. 9a) reveal the impact of the averaging period on these statistics, for which the bias is not nearly as sensitive as is the variance (Fig. 9b). The bias is only slightly changed, but the error markedly decreases by the collapse in spread for a longer averaging period.

Figure 10 shows the domainwide distributions of QuikSCAT and COAMPS correlation *R* for 1-, 5-, and 29-day averaging. At offshore locations, averaging pe-

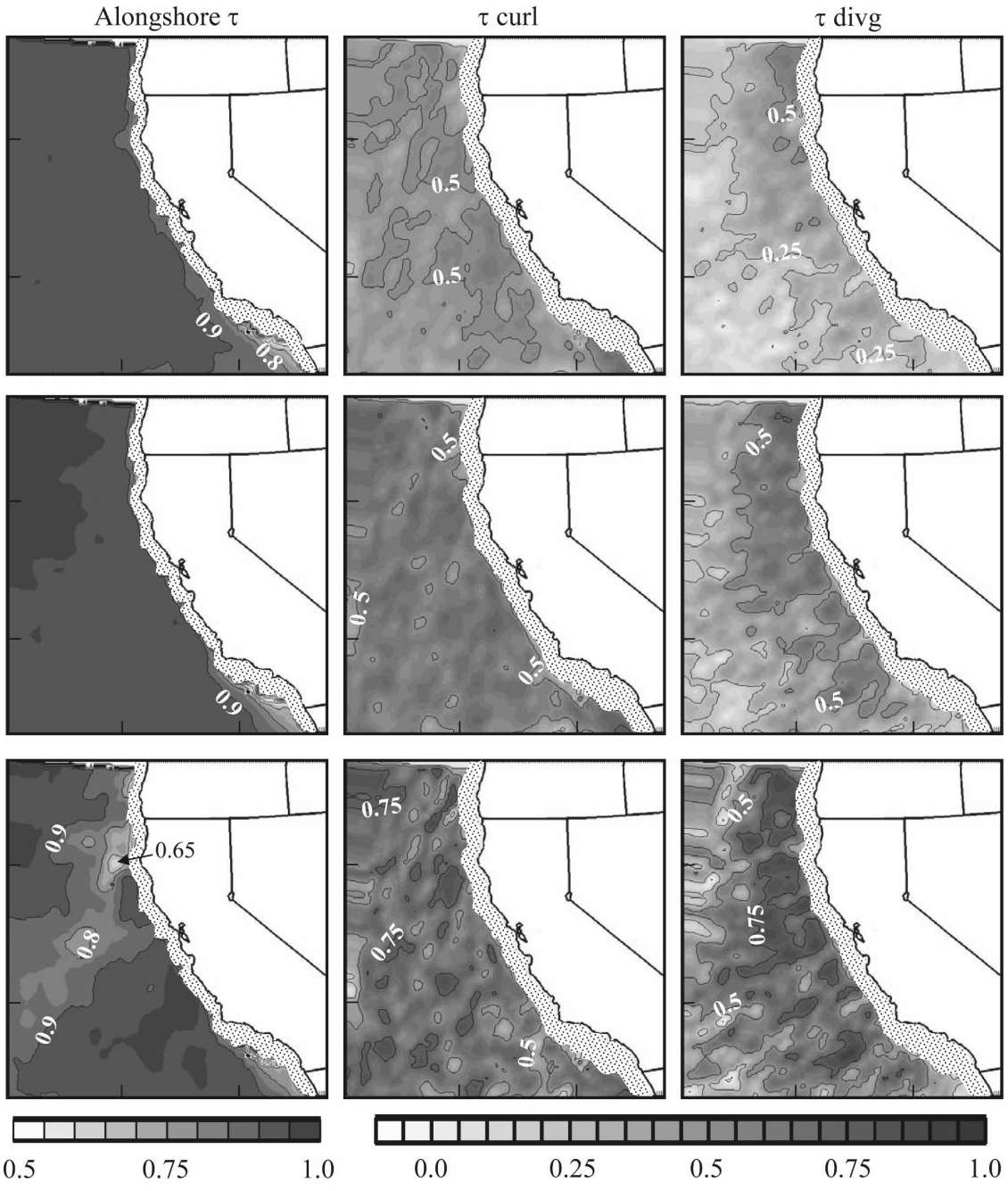

FIG. 10. Correlation maps between QuikSCAT and COAMPS of alongshore (left) wind stress (contour interval 0.1), (middle) wind stress curl, and (right) wind stress divergence (contour interval 0.25): (top to bottom) 1-, 5-, and 29-day averages. The stippled area along the coast masks the region without satellite data.

riods as low as 1 day produce $R \cong 0.9$ for alongshore wind stress, while yielding $R \cong 0.5$ for the gradient fields (weaker in the offshore regions for divergence because of the very small values west of the CA Current). Patchy areas of WSC and WSD have greater correlation approaching $R \cong 0.7$, demonstrating improvement over the NOAA North American Mesocale model (NAM) (formerly the Eta Model) for which R values are generally less than 0.5 (see Fig. 15 of CSS07). For an averaging period of 5 days, QuikSCAT and COAMPS correlations rapidly improve to $R \cong 0.7$, and by 29 days to $R \cong 0.9$ across much of the ocean domain.

With a longer averaging period, alongshore wind stress R values paradoxically diminish slightly in a wide

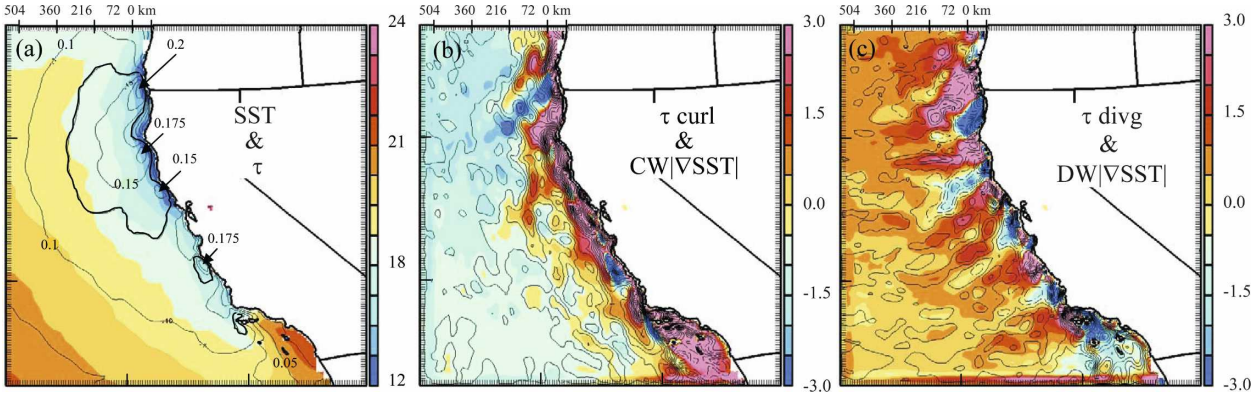

FIG. 11. Summertime mean temperature and wind fields: (left) SST (°C, color shading) and wind stress (N m^{-2}, contour interval of 0.025), (middle) wind stress curl [N m^{-2} $(10^4$ km$)^{-1}$, color shading] and crosswind SST gradient [°C (100 km)$^{-1}$, contour interval of 0.3], and (right) wind stress divergence [N m^{-2} $(10^4$ km$)^{-1}$, color shading] and downwind SST gradient [°C (100 km)$^{-1}$, contour interval of 0.3]. Negative contours are dashed and positive contours are solid.

band extending southwestward from the headlands of Cape Mendocino. This reduced correlation is related to weaker wind stress variability for 29-day averaging (see Fig. 6c). We return to this point in the next section. The overall agreement utilizing a 29-day averaging period provides confidence for conducting the subsequent analysis to ascertain the degree of air–sea interaction present in COAMPS model fields on monthly time scales.

5. Air–sea interaction

We quantify the degree of air–sea interaction in COAMPS by computing correlations and coupling coefficients between COAMPS analyzed SST gradient fields and forecast wind stress derivative fields.

a. Correspondence and correlations

Overlay of the mean fields reveals the air–sea interaction represented by COAMPS analyses and forecasts. The north coast's wind stress maximum coincides with a broad expanse of the coldest SST (Fig. 11a), revealing evidence of the atmosphere forcing the ocean in the form of wind-driven coastal upwelling. Note, however, that the wind stress decreases over the coldest water near the coast, resulting in positive WSC near shore that is consistent with the SST influence on surface winds discussed below (see also Perlin et al. 2007). As documented by Strub and James (2000), wind-stress-driven Ekman transport tends to draw cold core eddies and filaments westward as the upwelling season progresses. Away from the coast, relatively subtle covariations in the mean patterns of SST and wind stress suggest oceanic forcing of the atmosphere. Tight coupling between the two is readily apparent in individual 29-day averages, often showing warm water intrusions between Cape Blanco and Mendocino corresponding to locations of accelerated winds and fingers of cold SST west of both capes corresponding to decelerated winds, extending southwestward up to 300 km from shore (Fig. 2c).

The relatively small scale air–sea interaction becomes evident with the spatial high-pass filtering inherent in the SST gradient and derivative wind stress fields, which draw out the relationships between WSC and CWSST and between WSD and DWSST. Away from the immediate orographic effects of land and topography, mean WSC varies with the underlying mean CWSST such that negative (positive) WSC correspond to CWSST less (greater) than 1.0°C (100 km)$^{-1}$ (Fig. 11b). The lack of negative CWSST is because of the monotonic offshore increase of SST in the summertime mean. Because there is no such systematic alongshore structure in the mean SST field, the interaction between mean WSD and DWSST is much clearer, revealing collocated perturbations of the same sign for each field (Fig. 11c). Large-scale background forcing, emphasized in the mean fields, can mask the small-scale interaction that is so obvious in the individual 29-day averages (see Fig. 2). For example, negative WSC over the ocean interior is generated by the position and orientation of the large-scale atmospheric low-level jet, while the collocated expanse of positive CWSST results from the large-scale east–west offshore SST gradient noted above.

To quantify the correspondence between the wind stress derivative fields and their corresponding SST gradient counterparts, correlations are computed from 29-day averages (Fig. 12). They are about 20% greater

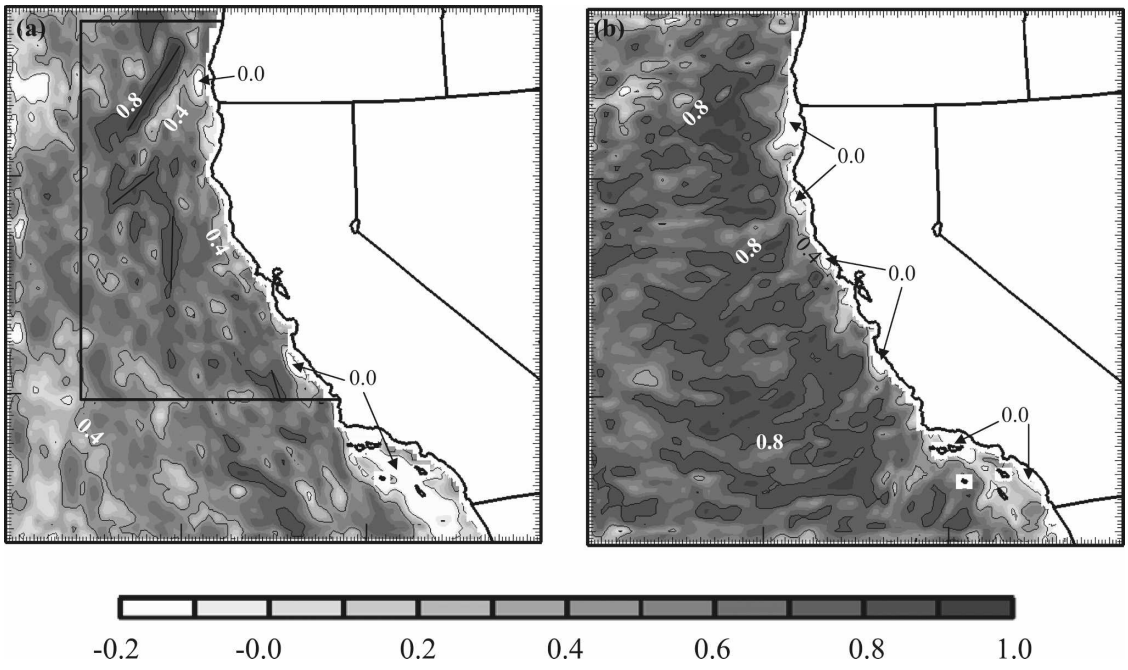

FIG. 12. Correlation maps between summertime wind stress derivative and SST gradient fields computed from 29-day averages, (left) between wind stress curl and crosswind SST gradient magnitude and (right) between wind stress divergence and downwind SST gradient magnitude. Contour interval is 0.4; locations and region denoted by black lines are discussed in the text.

than those reported by CSS07, which is likely the result of the superior spatial resolution of the COAMPS SST fields used here compared with the 56-km footprint of the AMSR measurements used by CSS07. Most regions have $R > 0.7$, but there are obvious departures from the strong air–sea interaction shown here. In coastal locations the wind stress and derivative fields are often dominated by topographic forcing of much larger magnitude than that imposed by the underlying SST perturbation. The coastal wind stress and derivatives display the hallmarks of expansion fans and compression jumps that form as the MABL responds to bends in the coastline. Several previous studies have demonstrated the hydraulic nature of COAMPS MABL summertime forecasts along the U.S West Coast and validated their robustness with aircraft data (Rogers et al. 1998; Haack et al. 2001; Burk and Haack 2000; Dorman et al. 1999). Downwind of all major capes and headlands, SST gradient magnitudes are negatively correlated to their corresponding wind stress derivative field (Fig. 12b), as is also the case in the Southern California Bight where the atmospheric flow is strongly modulated by the topography, Channel Islands, and sea/land breeze forcing.

Air–sea interaction is strongest upwind and offshore of the leading edge of expansion fans. Here the winds within supercritical flow do not experience the effects of the bend in the topography, so are much more responsive to the underlying SST. Additionally, CSS07 point out the impact of expansion fan wind stresses transporting cold filaments westward so that SST fronts also become intensified in this region. Both conditions contribute to bands of highly correlated WSC and CWSST upwind and offshore of expansion fans. In the correlation map between COAMPS WSC and CWSST (Fig. 12a), four such bands, indicated by black lines, are consistent with this interpretation; all four are associated with positive WSC and CWSST anomalies.

The correlation patterns are patchy in nature, having adjacent regions of high/low correlation. The spatial structure is quite similar to the monthly standard deviations (Figs. 5e,f and 7e,f) and the correlation maps between COAMPS and QuikSCAT (Fig. 10). The source of such inhomogeneity is related to the dynamic range of the gradient fields. Locations with a weak residual SST gradient magnitude are unlikely to illicit a strong dynamical response in the derivative wind stress fields, so that regions of large variance have greater correlation than regions of low variance. Figure 13 confirms this assertion, showing the mean 29-day-average STD of the CWSST (DWSST) as a function the correlation between CWSST and WSC (DWSST and WSD). Given that the isotherms are mostly aligned alongshore, STDs are larger for the crosswind component than for the downwind component. (Note the

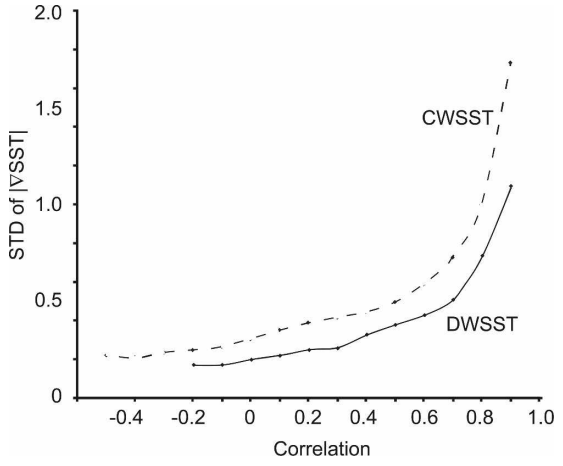

FIG. 13. Mean values of cross- or downwind SST gradient magnitude STD [°C (100 km)$^{-1}$] in each correlation bin computed from 29-day averages. The solid line is the mean STD of the downwind SST (SST) gradient magnitude in each correlation bin between divergence and DWSST; dashed line is the mean STD of the crosswind SST (CWSST) gradient magnitude in each correlation bin between curl and CWSST.

small variance for correlations less than ~0.3 and the rapid increase in variance for correlations above ~0.5.)

b. Coupling coefficients

The high correlations in Fig. 12 indicate a strong linear relationship between WSC and CWSST and between WSD and DWSST. These relationships are quantified by computing the linear slopes of mean values constructed from binned scatterplots of overlapping 29-day averages. In the manner described by CSS07, the anomaly WSC (WSD) (difference between each 29-day average and the summertime mean) is binned according to its corresponding anomaly CWSST (DWSST) for grid points lying within the region shown in Fig. 12a, excluding points within 100 km of the coast (Fig. 14). These grid points were chosen to be consistent with the region selected by CSS07 in computing their coupling coefficients from satellite data (their Fig. 7). The dot is the mean value and the line is plus/minus one standard deviation for all values within each bin. The linear fit to the mean values yields the slope s or coupling coefficient. The binned scatterplots from QuikSCAT data are also shown for comparison to COAMPS. Both model and QuikSCAT results are obtained by using the twice-daily fields interpolated to a common 0.25° grid.

Because the COAMPS SST analysis over a 29-day averaging period retains a higher spatial resolution and accuracy than the AMSR SST fields analyzed by CSS07, it is used to compute the coupling coefficients for both QuikSCAT and COAMPS. Thus, any discrepancy between the two sets of coupling coefficients is due entirely to the atmospheric response in the model. In comparison to the coupling inferred from QuikSCAT data, COAMPS underestimates the curl response by 14% and the divergence response by 26%, and standard deviations for both are about one-third less in COAMPS. This result suggests that the model may possess too little mixing, an issue recently addressed by Song et al. (2008). There are obvious differences between the values in Fig. 14 and those obtained by CSS07 (their Fig. 7). The error bars are smaller in CSS07 because their standard deviations are of the individual 29-day averages within each bin. Further, slopes are ~10% stronger in CSS07, attributable mostly to the coarse-resolution AMSR SST fields used in their calculation, which yields less resolved features and hence weaker gradients compared to the COAMPS SST analysis.

It is noteworthy that, for both QuikSCAT and COAMPS, the coupling coefficients for WSD are larger than for WSC. This has been found to be the case throughout the World Ocean (Chelton et al. 2001, 2004; O'Neill et al. 2003; Maloney and Chelton 2006; CSS07). O'Neill et al. (2008, manuscript submitted to *J. Climate*) have recently shown that this difference is due to the relatively small influence of SST on wind direction that results in anticyclonic turning over warm water and cyclonic turning over cold water. The net effect of these directional changes is to augment the WSD and reduce the WSC that are generated by the stronger wind speed response to SST, thus resulting in somewhat larger coupling coefficients for WSD than for WSC.

Air–sea coupling represented in other models has also been documented over the California Current. CSS07 found minimal air–sea interaction in the 12-km gridded NAM fields, which they attribute to inadequacies in the real-time global (RTG) SST analysis. The 9-km fifth-generation Pennsylvania State University–National Center for Atmospheric Research Mesoscale Model (MM5) gridded fields from June 1999 analyzed by Koračin et al. (2004) produce an average wind stress curl that is mostly negative and almost completely lacking in spatial variability offshore, due at least in part to the poor quality of the SST fields used as the surface boundary condition in their simulations. The coupling coefficients from the Scripps Coupled Ocean–Atmosphere Regional (SCOAR) model, which has horizontal grid spacing of 7 km for the ocean and 16 km for the atmosphere, are about 80% smaller than from COAMPS (Seo et al. 2007). Moreover, in a study of six global climate models, only three contained sufficient

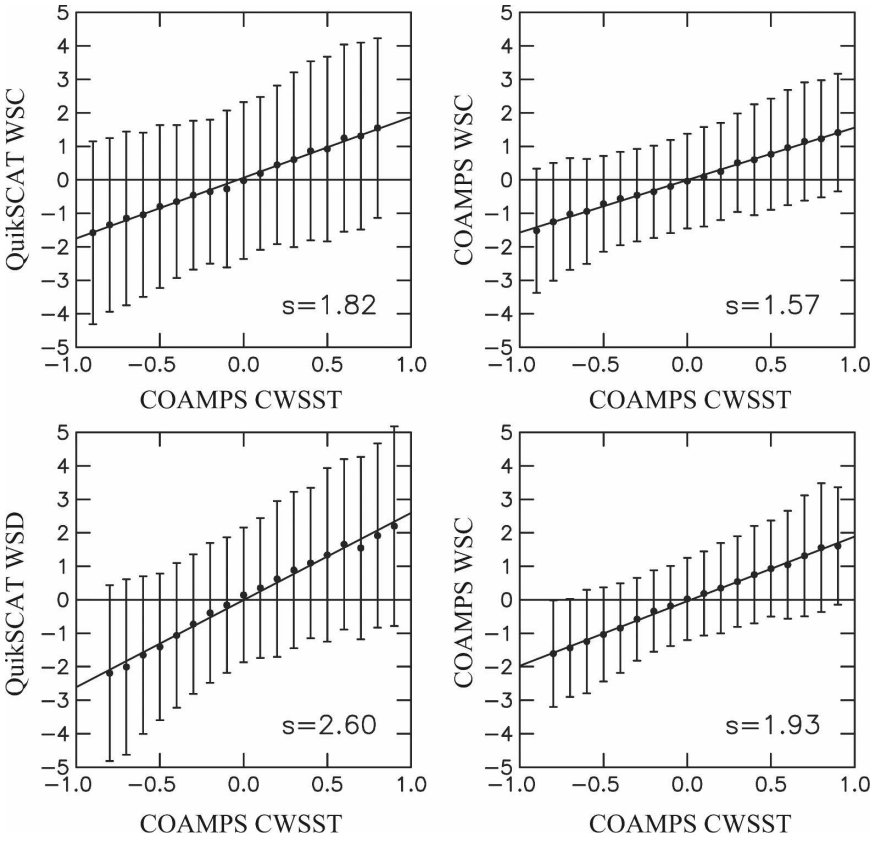

FIG. 14. Binned scatterplots of anomaly wind stress derivatives [N m^{-2} (10^4 km)$^{-1}$] vs anomaly SST gradient magnitudes [°C (100 km)$^{-1}$] computed from 29-day averages, (top) wind stress curl vs crosswind SST gradient and (bottom) wind stress divergence vs downwind SST gradient. For comparison with (right) COAMPS results, QuikSCAT wind stress derivatives are binned according to (left) COAMPS SST gradient magnitudes. Within each bin, the dot is the mean and the line is ±1 STD. The slope *s* is the least squares fit of the mean values. See text for details.

horizontal resolution to produce clear linear relationships between the wind stress and SST fields and with coupling coefficients only about half those derived from observations (Maloney and Chelton 2006). Over the CA Current, the COAMPS model thus demonstrates much closer agreement with satellite-observed air–sea interaction compared with other coupled or uncoupled regional, mesoscale, or climate models.

c. Fluxes

In this section, COAMPS surface heat fluxes are presented, as they are the mechanism by which the SST is coupled to the overlying atmosphere. The sign convention is such that positive values indicate upward heat flux. In 29-day averages, these mean fields contain spatial variability predominately imposed by the SST. The correspondence is clearly evident in the gradient magnitudes of heat flux overlaid with contours of SST gradient magnitude for the same two center dates discussed in section 3 (Fig. 15). Here, latent heat flux (LHF) is shown, although sensible heat flux (SHF) spatial structure is equally compatible with that of the SST. In the summertime mean flux fields (Figs. 16a,b), undulations in the mean patterns mimic those of the mean SST field (Fig. 4a), revealing four preferential locations of weak fluxes extending offshore at or downwind of each topographic cape and point. Stronger fluxes penetrate shoreward over warm SST intrusions generally located between the promontories.

The LHF is more sensitive to variations in SST than SHF, stemming from the functional relationship of saturation specific humidity to SST. Owing to cold coastal SST and a nearly saturated near-surface atmosphere, mean LHFs are small all along the coast. Mean SHFs transition from downward north of San Francisco Bay to upward south of the Bay. These fields are similar in pattern and magnitude to the July 1999 fluxes shown in Haack et al. (2005), but with less spatial structure,

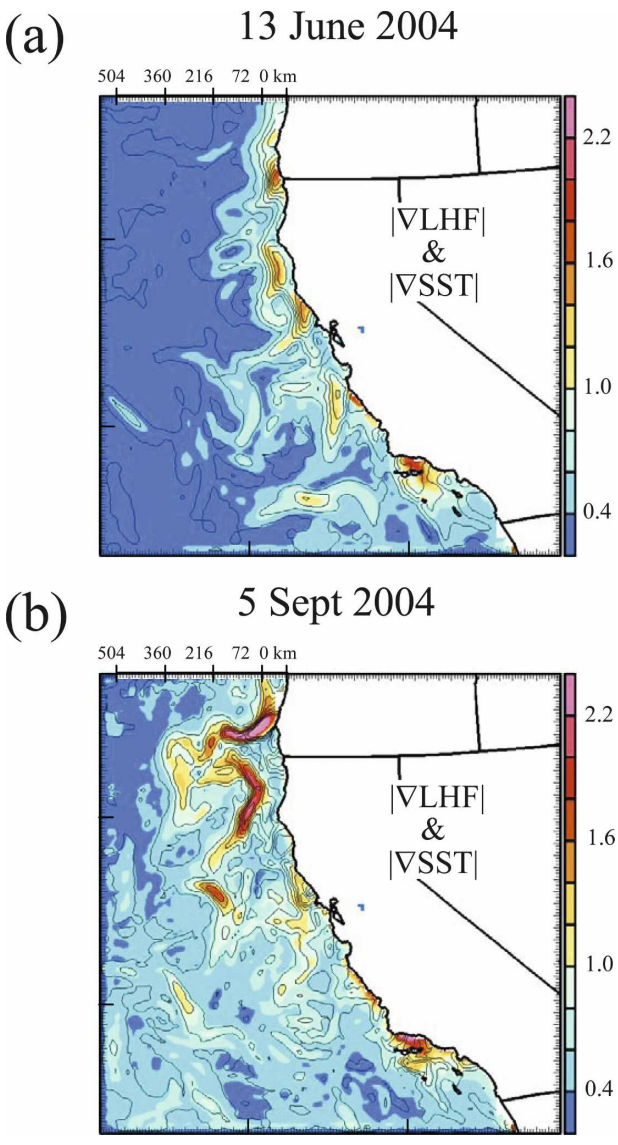

FIG. 15. Example 29-day averages of LHF gradient magnitude [W m^{-2} $(km)^{-1}$, color shading] and SST gradient magnitude [°C $(100\ km)^{-1}$, contour interval of 1.0] for center date (a) 13 Jun 2004 and (b) 5 Sep 2004.

largely due to the longer averaging in this study over the four summers of 2002–05. Since LHF is quite weak within ~75 km of the coast, hourly standard deviations are also small in this nearshore region where hourly SHF variance tends to be a maximum (Figs. 16c,d). The contrasting pattern in SHF fluctuations matches that of the wind stress (Fig. 6b) and emphasizes the role of diurnal variation in low-level wind speeds in controlling the SHF near shore. Here SHF can be modified by up to 20 W m^{-2} and altered from downward to upward flux by the diurnal changes in wind speed and air temperature.

Deviations in the surface fluxes on monthly time scales are reflected in the 29-day-average STD (Figs. 16e,f). These fields display patterns similar to the STD from hourly fields but with more structure and localized regions of variability offshore. Patches of high/low deviation are replicated by the SST STD pattern (Fig. 4e) everywhere except west of the three primary expansion fans at Capes Blanco and Mendocino and Point Sur. These locations have greater variance in the fluxes on monthly time scales because of the large deviations in wind stress (Fig. 6c) associated with warm intrusions of SST, once again highlighting tight coupling between the ocean and atmosphere.

In most cases, perturbations in LHF are positively correlated to those of SST, in agreement with the SCOAR coupled modeling results of Seo et al. (2007) for the CA Current. Their sign convention for surface fluxes is opposite that of COAMPS, resulting in a negative slope between LHF and SST. Coupling coefficients between gradient LHF and gradient SST 29-day-average anomalies are considered for the two regions shown in Fig. 16b. Comparisons with Seo et al. (2007) indicate similar coefficients in the southern region (slope = 17.7; STD ±6.5 to ±10.3) but 80% stronger coupling in COAMPS in the northern region (slope = 20.7; STD ±7.4 to ±11.1), consistent with the stronger COAMPS WSC and WSD coupling coefficients noted in the previous section.

The distribution of mean and 29-day-average anomaly fluxes is shown in Fig. 17. The dynamic ranges of anomalies of both SHF and LHF are about the same as the dynamic ranges of the overall means (~20 W m^{-2} for SHF and ~60 W m^{-2} for LHF). This implies that the effect of SST-induced perturbations on the summertime mean heat flux field is $O(1)$. For a fully interactive ocean and atmosphere, the fluxes also influence the SST such that positive LHF and SHF perturbations, resulting from faster winds over warmer water, produce evaporative cooling and heat loss to the atmosphere (Zhang and McPhaden 1995). This negative feedback would likely reduce the dynamic range of flux anomalies in a two-way coupled model.

At issue is how the heat fluxes contribute to the structure and development of the CA Current. Marchesiello et al. (2003) suggest that Ekman transport helps to maintain the current, despite the distribution of surface heat fluxes, which would tend to weaken SST gradients. Edwards and Kelly (2007) also examine the heat budget of the CA Current, finding no signature in any component of the heat flux associated with the cross-shore grown of the current. A limitation of both studies is the coarse spatial resolution of the surface

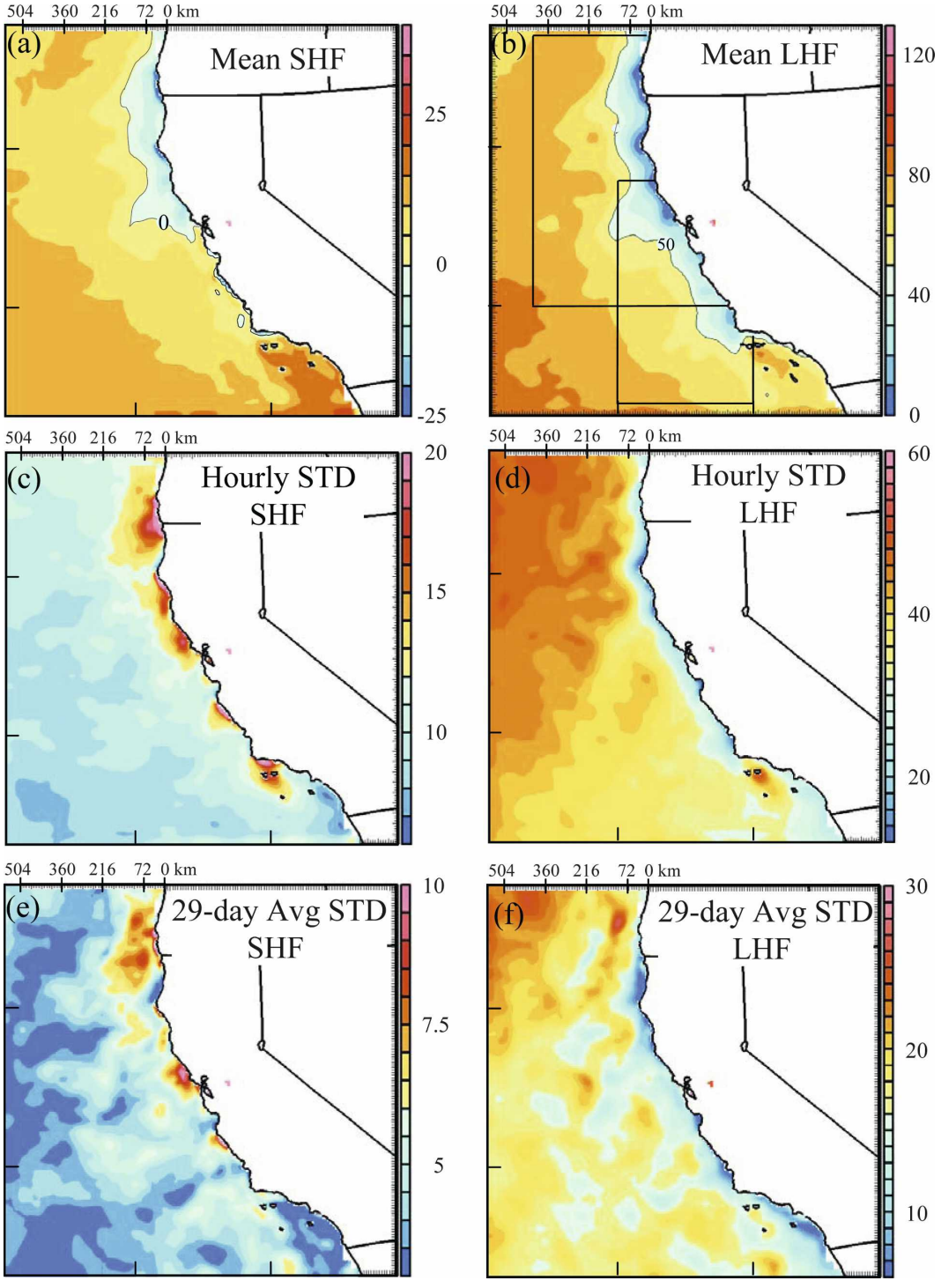

FIG. 16. Surface (left) sensible and (right) latent heat flux means and STDs (W m^{-2}): (top to bottom) Mean, hourly STD, and 29-day average STD. Regions denoted by black lines in Fig. 14b are discussed in section 5c.

forcing or fields analyzed. In a mesoscale coupled modeling system, the role of dynamically evolving, fully interactive heat fluxes on the ocean circulation can be considered along with that of a spatially complex wind stress and wind stress curl field (see section 6). Moreover, this system would permit the evaluation of improved resolution on the ocean energy and heat budgets.

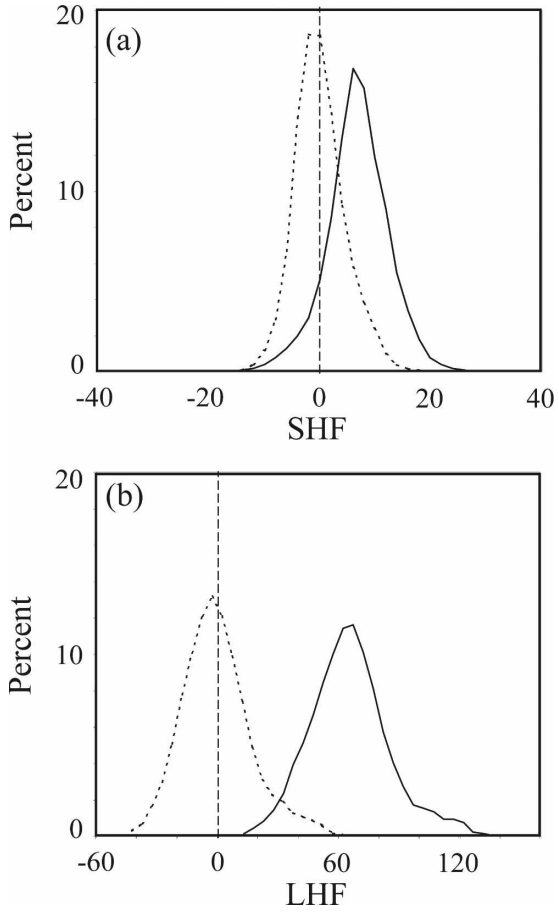

FIG. 17. Mean (solid) and anomaly (dotted) distributions of surface (top) sensible and (bottom) latent heat flux (W m^{-2}) computed from 29-day averages over the box shown in Fig. 12a.

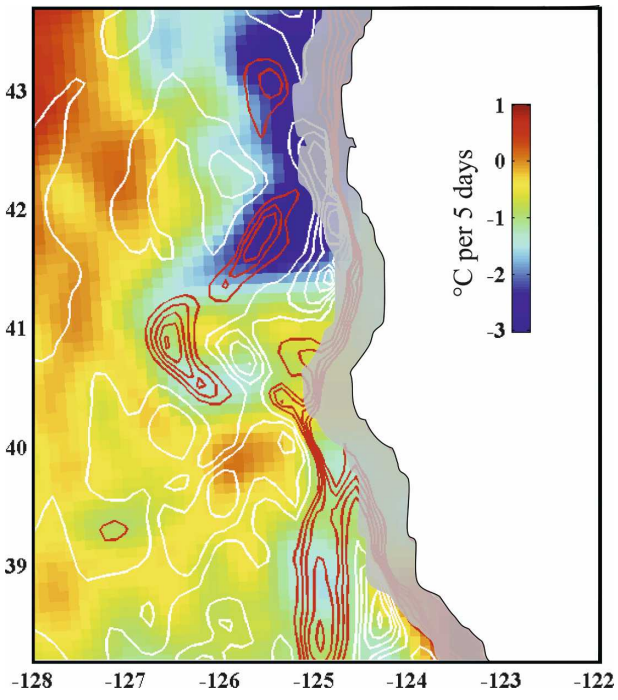

FIG. 18. SST change (°C per 5 days, color shading) and 5-day-average wind stress curl [N m^{-2} $(10^4$ km$)^{-1}$, contours] from 1200 UTC 27 Jun to 2 Jul 2004. Contours are shown in the range ±15 every 3 [N m^{-2} $(10^4$ km$)^{-1}$] with positive values in red and negative values in white; gray shading near the coast masks the topographically generated coastal curl.

6. Discussion

This paper focuses on the role of small-scale spatial variations in SST in modulating the near-surface atmospheric wind field over the CA Current; however, in a fully coupled system Ekman pumping associated with the wind stress curl also exerts a feedback influence on the SST, producing localized regions of enhanced upwelling and downwelling. For a northerly wind direction, the strongest SST-induced positive WSC resides along the western side of a north–south oriented portion of SST front. The Ekman upwelling associated with this atmospheric forcing would tend to draw the SST front westward. Edwards and Kelly (2007) found broad evidence of this coupling in their study of satellite observations, which showed that the region of positive wind stress curl widens at the same gradual rate as the CA Current. Hence, perturbations in WSC likely contribute to the movement of SST fronts, the meandering of warm and cold SST filaments, and perhaps the formation of eddies. Moreover, this positive feedback between SST and WSC could promote stronger coupling.

To illustrate this process, we consider a region offshore just north of Cape Mendocino containing a strong SST front oriented roughly north–south between about 40.3° and 41.4°N, 126°W and 127°N. Aside from the masked, topographically enhanced WSC near the coast, the region of strongest Ekman pumping is shown by red contours in Fig. 18 corresponding to the largest values of 5-day-average WSC. These contours coincide with the regions of greatest cooling, presumably due to curl-driven Ekman upwelling over the same 5-day period: Notice the cold SST filament between Capes Blanco and Mendocino that has developed a counterclockwise eddy centered at about 41°N, 126.2°W. Localized regions of positive and negative WSC may have contributed to the development of this eddy. Our analysis is limited since fully interactive air–sea feedbacks can only be provided by a two-way coupled model, which will be the subject of future work.

Of additional interest is the prominence of SST influence on the wind field in the nearshore zone, which can be assessed with COAMPS fields. Evidence of coupling was found by Perlin et al. (2007), who show reduced wind stress and increased WSC due to colder

coastal SSTs. However, abrupt spatial variations in wind stress are also driven by sea/land breezes and by the atmospheric boundary layer response to topographic promontories, resulting in anomalies in the wind stress derivatives that form independent of the underlying SST. Because both diurnal and orographic forcing exert strong influence on low-level coastal flows, we anticipate a reduction in the influence of SST along the coast compared to offshore, as demonstrated by lower correlations in Fig. 12.

To quantify the coastal air–sea interaction, we consider an ~100 km swath (11 grid points) along the coast between latitudes 35° and 45°N but ignore the two grid points closest to shore. Grid points within ~20 km of the coast are eliminated from the analysis because of the potential for error in the wind stress derivatives. Grid resolution and many other factors limit the ability of numerical models to capture the precise strength and variability of nearshore gradients including, for example, changes in surface roughness, surface fluxes, mesoscale pressure gradients, turbulence, and clouds. Validation of COAMPS wind stress curl for the 9-km U.S. West Coast domain has been performed in two studies. Pickett and Paduan (2003) found that COAMPS wind gradients near Point Arena are within 20% of those computed from a limited set of buoy and satellite observations. More recently, an assessment of wind stress curl during the Adaptive Ocean Sampling Network (AOSN) field campaign in Monterey Bay (Paduan et al. 2006) suggests that COAMPS 9-km curl is too large within two grid points of shore based on overwater aircraft measurements, an error attributed largely to the 9-km grid spacing. Additional verification of nearshore wind speed gradients continues to be the subject of ongoing investigations.

The WSC and CWSST anomalies and WSD and DWSST anomalies nearshore maintain a linear relationship (not shown) but with reduced slopes compared to the strong air–sea interaction found offshore (Fig. 14). The reduction in WSC/CWSST slope is approximately 20% to $s = 1.39$, and the reduction in WSD/DWSST slope is approximately 40% to $s = 1.37$. The STDs within each bin are about four times larger than in Fig. 14. In the coastal band, the coupling coefficients are essentially the same for both the WSC and WSD, contrary to offshore (Fig. 14). This effect is most likely an indication of the topographic constraints on wind direction.

7. Conclusions

The present study demonstrates COAMPS ability to replicate the pronounced air–sea interaction over the CA Current in summertime that was documented from satellite observations by Chelton et al. (2007). We have examined 4-yr summertime statistics of the one-way coupling between COAMPS analyzed SST and forecast wind stress. Although hourly deviations are evaluated and compared to monthly deviations, the emphasis for air–sea interaction is on the longer monthly time scales as revealed by analysis of observational data for this region (Chelton et al. 2007). Examination of individual monthly averages shows small-scale features in the derivative wind stress fields that mimic spatial variations in the SST gradient fields. Correlation maps indicate broad regions where these fields have a high correspondence with large coupling coefficients that indicate a clear linear relationship between perturbations in the ocean and atmosphere. The coefficients are considerably larger than the relatively weak coupling previously documented for other atmospheric models but are about 15%–25% lower than those computed from satellite retrievals.

The larger coupling coefficients derived from COAMPS fields relative to other mesoscale, regional and climate models illustrates the importance of the quality of the SST boundary condition in reproducing realistic air–sea interaction features. The model's robustness hinges on the SST analysis (Cummings 2005) that, on the monthly time scales of interest here, yields accurate, high-resolution SST and SST gradient fields in comparison to other available sources of data. The strongest air–sea interaction occurs where monthly averaged SST gradient magnitudes are greatest, which tends to track north over the upwelling season in tandem with the shift in position of the large-scale atmospheric low-level jet. Bands of strong interaction preferentially occur upwind and offshore of MABL expansion fans (localized atmospheric wind maxima near the coast that form in the lee of topographic promontories). In these locations atmospheric winds are more responsive to the SST forcing, and oceanic fronts are strengthened by the strong expansion fan wind forcing.

Topographic and diurnal effects reduce COAMPS coupling coefficients by 20%–40% within the 100-km-wide coastal zone, while maintaining a linear relationship and evidence of air–sea interaction. The eastern sides of expansion fans (localized nearshore wind speed maxima) have very low or negatively correlated SST gradients and wind stress derivatives, while the western sides are positively correlated and contain strong negative curl that in a fully coupled system imposes persistent downwelling due to Ekman pumping. We speculate that this atmospheric forcing contributes to the shoreward penetration of warm SST intrusions downwind and offshore of coastal headlands. The regions

subject to expansion fan wind maxima tend to have a large variance in wind stress as well as in latent and sensible heat flux, indicative of dynamic processes there.

In examining the role of SST on surface fluxes, we find that gradients of sensible and latent heat flux vary in concert with those of the SST over a large portion of the model domain. Anomaly flux distributions elucidate the large dynamical range of SST-forced flux perturbations compared to the mean flux distribution, demonstrating that the SSTs have a first-order effect on the mean heat flux fields. The similarity in spatial patterns clearly indicates that perturbations in the fluxes are associated with the SST field and it is these surface fluxes that communicate the SST forcing to the atmospheric surface layer. Evaluation of COAMPS SST analysis and the one-way coupled atmospheric response suggests that oceanic fronts, meanders, and eddies may be responsive to the small-scale structure of the atmospheric flow field, which is shown to be sensitive to spatial features of SST. Hence, this study lends further support for considering the CA Current region a fully coupled ocean–atmosphere system during summertime.

Acknowledgments. We are grateful for the effort of Dr. James Cummings, who designed the SST analysis used by COAMPS, and for the input of Drs. Shouping Wang and Jeffrey Paduan who each offered suggestions in shaping the content of the paper pertinent to their research. This work was supported by the Office of Naval Research, Program Elements 0601153N, NASA Grant NAS 5-32965, and Contracts 1283973 and 1283976 from the NASA Jet Propulsion Laboratory for funding of Ocean Vector Winds Science Team activities.

REFERENCES

Baker, N. L., 1992: Quality control for the navy operational atmospheric database. *Wea. Forecasting,* **7,** 250–261.

Barker, E. H., 1992: Design of the navy's multivariate optimum interpolation analysis system. *Wea. Forecasting,* **7,** 220–231.

Burk, S. D., and T. Haack, 2000: The dynamics of wave clouds upwind of coastal orography. *Mon. Wea. Rev.,* **128,** 1438–1455.

——, ——, and R. M. Samelson, 1999: Mesoscale simulation of supercritical, subcritical, and transcritical flow along coastal topography. *J. Atmos. Sci.,* **56,** 2780–2795.

Castelao, R. M., R. P. Mavor, J. A. Barth, and L. C. Breaker, 2006: Sea surface temperature fronts in the California Current System from geostationary satellite observations. *J. Geophys. Res.,* **111,** C09026, doi:10.1029/2006JC003541.

Chelton, D. B., 2005: The impact of SST specification on ECMWF surface wind stress fields in the eastern tropical Pacific. *J. Climate,* **18,** 530–550.

——, and M. H. Freilich, 2005: Scatterometer-based assessment of 10-m wind analyses from the operational ECMWF and NCEP numerical weather prediction models. *Mon. Wea. Rev.,* **133,** 409–429.

——, and Coauthors, 2001: Observations of coupling between surface wind stress and sea surface temperature in the eastern tropical Pacific. *J. Climate,* **14,** 1479–1498.

——, M. G. Schlax, M. H. Freilich, and R. F. Milliff, 2004: Satellite measurements reveal persistent small-scale features in ocean winds. *Science,* **303,** 978–983.

——, M. H. Freilich, J. M. Sienkiewicz, and J. M. Von Ahn, 2006: On the use of QuikSCAT scatterometer measurements on surface winds for marine weather prediction. *Mon. Wea. Rev.,* **134,** 2005–2071.

——, M. G. Schlax, and R. M. Samelson, 2007: Summertime coupling between sea surface temperature and wind stress in the California Current System. *J. Phys. Oceanogr.,* **37,** 495–517.

Cummings, J. A., 2005: Operational multivariate ocean data assimilation. *Quart. J. Roy. Meteor. Soc.,* **131,** 3583–3604.

Dorman, C. E., 1985: Hydraulic control of the northern California marine layer (abstract). *Eos, Trans. Amer. Geophys. Union,* **66,** 914.

——, D. P. Rogers, W. Nuss, and W. T. Thompson, 1999: Adjustment of the summer marine boundary layer around Pt. Sur, California. *Mon. Wea. Rev.,* **127,** 2143–2159.

Edwards, K. A., and K. A. Kelly, 2007: A seasonal heat budget across the extent of the California Current. *J. Phys. Oceanogr.,* **37,** 518–530.

——, A. M. Rogerson, C. D. Winant, and D. P. Rogers, 2001: Adjustment of the marine atmospheric boundary layer to a coastal cape. *J. Atmos. Sci.,* **58,** 1511–1528.

Fairall, C. W., E. F. Bradley, D. P. Rogers, J. B. Edson, and G. S. Young, 1996: Bulk parameterization of air-sea fluxes for tropical ocean-global atmospheric coupled-ocean atmosphere response experiment. *J. Geophys. Res.,* **101,** 3747–3764.

Friehe, C. A., and Coauthors, 1991: Air-sea fluxes and surface layer temperatures around a sea surface temperature front. *J. Geophys. Res.,* **96,** 8593–8609.

Haack, T., and R. M. Hodur, 1996: A coupled ocean/atmosphere modeling study of an arctic lead. *The Air-Sea Interface Radio and Acoustic Sensing, Turbulence and Wave Dynamics,* M. A. Donelan, W. H. Hui and W. J. Plant, Eds., The Rosenstiel School of University of Miami, 789 pp.

——, S. D. Burk, C. E. Dorman, and D. P. Rogers, 2001: Supercritical flow interaction within the Cape Blanco–Cape Mendocino orographic complex. *Mon. Wea. Rev.,* **129,** 688–708.

——, ——, and R. M. Hodur, 2005: U.S. West Coast surface heat fluxes, wind stress, and wind stress curl from a mesoscale model. *Mon. Wea. Rev.,* **133,** 3202–3216.

Hayes, S. P., M. J. McPhaden, and J. M. Wallace, 1989: The influence of sea surface temperature on surface wind in the eastern equatorial Pacific: Weekly to monthly variability. *J. Climate,* **2,** 1500–1506.

Hodur, R. M., 1997: The Naval Research Laboratory's Coupled Ocean/Atmosphere Mesoscale Prediction System (COAMPS). *Mon. Wea. Rev.,* **125,** 1414–1430.

Hogan, T. H., and T. E. Rosmond, 1991: The description of the U.S. Navy Operational Global Analysis and Prediction System's spectral forecast model. *Mon. Wea. Rev.,* **119,** 1786–1815.

Jury, M. R., and N. Walker, 1988: Marine boundary layer modification across the edge of the Agulhas Current. *J. Geophys. Res.,* **93,** 647–654.

Kindle, J. C., R. M. Hodur, S. deRada, J. Paduan, L. Rosenfeld, and F. Chavez, 2002: A COAMPS reanalysis for the Eastern Pacific: Properties of the diurnal sea breeze along the central California coast. *Geophys. Res. Lett.,* **29,** 2203, doi:10.1029/2002GL015566.

Koračin, D., C. E. Dorman, and E. P. Dever, 2004: Coastal perturbations of marine-layer winds, wind stress, and wind stress curl along California and Baja California in June 1999. *J. Phys. Oceanogr.,* **34,** 1152–1173.

Louis, J. F., M. Tiedtke, and J. F. Geleyn, 1982: A short history of the operational PBL-parameterization at ECMWF. *Proc. Workshop on Planetary Boundary Parameterization,* Reading, United Kingdom, ECMWF, 59–79. [Available from ECMWF, Shinfield Park, Reading RG2 9AX, United Kingdom.]

Mahrt, L., D. Vickets, and E. Moore, 2004: Flow adjustments across sea-surface temperature changes. *Bound.-Layer Meteor.,* **111,** 553–564.

Maloney, E. D., and D. B. Chelton, 2006: An assessment of the sea surface temperature influence on surface wind stress in numerical weather prediction and climate models. *J. Climate,* **19,** 2743–2762.

Marchesiello, P., J. C. McWilliams, and A. Shchepetkin, 2003: Equilibrium structure and dynamics of the California Current System. *J. Phys. Oceanogr.,* **33,** 753–783.

Mooers, C. N. K., and A. R. Robinson, 1984: Turbulent jets and eddies in the California Current and inferred cross-shore transports. *Science,* **223,** 51–53.

O'Neill, L. W., D. B. Chelton, and S. K. Esbensen, 2003: Observations of SST-induced perturbations of the wind stress field over the Southern Ocean on seasonal timescales. *J. Climate,* **16,** 2340–2354.

Paduan, J. D., and Coauthors, 2006: Headland-scale wind stress curl around Monterey Bay from aircraft and nested COAMPS model results (abstract). *Eos, Trans. Amer. Geophys. Union,* **87.**

Perlin, N., E. D. Skyllingstad, R. M. Samelson, and P. L. Barbour, 2007: Numerical simulation of air–sea coupling during coastal upwelling. *J. Phys. Oceanogr.,* **37,** 2081–2093.

Phoebus, P., and J. Goerss, 1992: The assimilation of marine surface data into the Navy Operational Global Atmospheric Prediction. *J. Mar. Technol. Soc.,* **26,** 63–77.

Pickett, M. H., and J. D. Paduan, 2003: Ekman transport and pumping in the California Current based on the U.S. Navy's high-resolution atmospheric model (COAMPS). *J. Geophys. Res.,* **108,** 3327, doi:10.1029/2003JC001902.

Pullen, J., J. D. Doyle, and R. P. Signell, 2006: Two-way air–sea coupling: A study of the Adriatic. *Mon. Wea. Rev.,* **134,** 1465–1483.

——, ——, T. Haack, C. Dorman, R. P. Signell, and C. M. Lee, 2007: Bora event variability and the role of air-sea feedback. *J. Geophys. Res.,* **112,** C03S18, doi:10.1029/2006JC003726.

Rogers, D. P., and Coauthors, 1998: Highlights of coastal waves 1996. *Bull. Amer. Meteor. Soc.,* **79,** 1307–1326.

Seo, H., A. J. Miller, and J. O. Roads, 2007: The Scripps coupled ocean–atmosphere regional (SCOAR) model, with applications in the eastern Pacific sector. *J. Climate,* **20,** 381–402.

Small, J., and Coauthors, 2008: Air–sea interaction over ocean fronts and eddies. *Dyn. Atmos. Oceans,* **45,** 274–319.

Song, Q., D. B. Chelton, and S. K. Esbensen, 2008: On the coupling between sea surface temperature and low-level winds in mesoscale numerical models. *J. Climate,* in press.

Spall, M. A., 2007: Midlatitude wind stress–sea surface temperature coupling in the vicinity of oceanic fronts. *J. Climate,* **20,** 3785–3801.

Strub, P. T., and C. James, 2000: Altimeter-derived variability of surface velocities in the California Current System: 2. Seasonal circulation and eddy statistics. *Deep-Sea Res. II,* **47,** 831–870.

Sweet, W., R. Fett, J. Kerling, and P. La Violette, 1981: Air–sea interaction effects in the lower troposphere across the north wall of the Gulf Stream. *Mon. Wea. Rev.,* **109,** 1042–1052.

Wallace, J. M., T. P. Mitchell, and C. Deser, 1989: The influence of sea surface temperature on surface wind in the eastern Equatorial pacific: Seasonal and interannual variability. *J. Climate,* **2,** 1492–1499.

Wang, S., Q. Wang, and J. Doyle, 2002: Some improvement of Louis surface flux parameterization. Preprints, *15th Symp. on Boundary Layer and Turbulence,* Wageningen, Netherlands, Amer. Meteor. Soc., 547–550.

Winant, C. D., C. E. Dorman, C. A. Friehe, and R. C. Beardsley, 1988: The marine layer off northern California: An example of supercritical channel flow. *J. Atmos. Sci.,* **45,** 3588–3605.

Xie, S.-P., 2004: Satellite observations of cool ocean–atmosphere interaction. *Bull. Amer. Meteor. Soc.,* **85,** 195–208.

Zhang, G. J., and M. J. McPhaden, 1995: The relationship between sea surface temperature and latent heat flux in the equatorial Pacific. *J. Climate,* **8,** 589–605.